Chemical Engineering Journal 421 (2021) 127740

Contents lists available at ScienceDirect

Chemical Engineering Journal

journal homepage: www.elsevier.com/locate/cej

# N-/S- dual doped C@ZnO: An excellent material for highly selective and responsive $NO_2$ sensing at ambient temperatures

Arunkumar Shanmugasundaram [a], Dong-Su Kim [a], Nguyen Duc Chinh [b], Jongsung Park [c], Yun-Jin Jeong [b], JunJi Piao [d], Dojin Kim [b], Dong Weon Lee [a,e,*]

[a] MEMS and Nanotechnology Laboratory, School of Mechanical Engineering, Chonnam National University, Gwangju 61186, Republic of Korea
[b] Nano Materials and Application Lab, Department of Materials Science and Engineering, Chungnam National University, Daejeon 305764, Republic of Korea
[c] Department of Precision Mechanical Engineering, Kyungpook National University, Sangju 37224, Republic of Korea
[d] Nano Energy Laboratory, Department of Materials Science and Engineering, Chonnam National University, Gwangju 61186, Republic of Korea
[e] Center for Next-Generation Sensor Research and Development, Chonnam National University, Gwangju 61186, Republic of Korea

ARTICLE INFO

*Keywords:*
N-/S- dual doped carbon
ZnO
$NO_2$ sensing
Ambient temperature sensor
High selectivity
Sensing mechanism

ABSTRACT

Nitrogen dioxide ($NO_2$) is an extremely toxic gas and harmful to human health and the environment. Inhalation of $NO_2$ reduces immunity to lung infections and causes respiratory problems such as wheezing, coughing, colds, flu, and bronchitis. To date, several sensors have been developed for the detection of $NO_2$. Indeed, the development of highly sensitive and selective room temperature sensor with rapid response and recovery time could be called an "innovation" for metal oxide-based gas sensors for environmental remedy applications. Herein, we prepared ZnO nanospheres (ZNS), nitrogen-doped carbon-coated ZnO spheres (NC@ZNS), sulfur-doped carbon-coated ZnO spheres (SC@ZNS), and nitrogen-sulfur dual doped carbon-coated ZnO spheres (NSC@ZNS) for $NO_2$ sensing. Among them, the NSC@ZNS exhibits excellent $NO_2$ sensing characteristics with the sensor response ($S_R = R_g/R_a$) of 730.4 and 31.2 at 100 and 25 °C, respectively. The limit of detection (LOD) of the NSC@ZNS sensor is ~21 ppb at ambient temperature. The NSC@ZNS hybrid nanocomposite sensor exhibits ultrafast response and recovery times of ~88 s and 305 s to 500 ppb of $NO_2$ at 25 °C. Besides, the NSC@ZNS sensor shows excellent selectivity to $NO_2$, which is ~31 times higher than other interfering gases. The enhanced sensing characteristics of the NSC@ZNS sensor is attributed to the synergy between the nitrogen-sulfur dual doped carbon and hierarchical mesoporous ZnO. The selective detection of $NO_2$ with significantly rapid response and recovery time at 25 °C makes for intriguing the promising practical applications of our proposed NSC@ZNS sensor.

## 1. Introduction

Nitrogen dioxide ($NO_2$) is an acidic, corrosive, and toxic gas mostly released from the combustion engines, fertilizer, and chemical industries [1,2]. $NO_2$ is a primary source of acid rain, and the acidification caused by acid rain severely affects the plants and other ecosystems [3]. According to the U.S. Environmental Protection Agency, the recommended air quality control for $NO_2$ exposure period is ~100 parts per billion (ppb) for 1 h, and the annual threshold limit is ~53 ppb [4,5]. Inhalation of $NO_2$ causes respiratory infections and asthma as it affects the human respiratory tract [6]. The long-term exposure to $NO_2$ causes chronic lung disease, genetic mutations, decreased female fertility, and death [7]. Therefore, the development of a high-sensitivity sensor for ppb level detection of $NO_2$ is required to safeguard the environment and human health [8,9].

Solid-state metal oxide gas sensors have received significant attention owing to their excellent sensitivity, ease of use, low fabrication cost, high surface area, and more effective reaction sites for the chemisorbed gas kinetic reaction [9–11]. To date, numerous metal oxide-based gas sensors have been developed for the selective and sensitive detection of $NO_2$ [12–16]. Among them, zinc oxide has considered a promising gas sensing material due to its outstanding chemical and thermal stability, high carrier density, and excellent sensitivity. For instance, wang *et al.* developed a hierarchical ZnO nanorod arrays based highly sensitive sensor and studied their temperature dependent $NO_2$ sensing characteristics at 200–225 °C [17]. Tamvakos *et al.* studied the $NO_2$ sensing

* Corresponding author at: MEMS and Nanotechnology Laboratory, School of Mechanical Engineering, Chonnam National University, Gwangju 61186, Republic of Korea.
*E-mail address:* mems@jnu.ac.kr (D.W. Lee).

https://doi.org/10.1016/j.cej.2020.127740
Received 23 July 2020; Received in revised form 14 October 2020; Accepted 12 November 2020
Available online 19 November 2020

characteristics of the ZnO thin-film transducers-based sensor at 200–400 °C [18].

To improve the sensitivity of the ZnO based $NO_2$ sensors, several research efforts have been focused on surface modification and doping catalytic material into the ZnO matrix [19,20]. For example, Xu *et al.* prepared $SnO_2$/ZnO heterostructures for the detection of $NO_2$ at ppb level. The developed sensor showed excellent sensitivity to 2 ppb of $NO_2$ at 300 °C [19]. Zhang *et al.* prepared Al-doped narcissus like ZnO for selective and sensitive detection of $NO_2$. The proposed sensing material showed a maximum $S_R$ of ~104 to 1 ppm of $NO_2$ at 240 °C, which was ~3-folds higher than a bare ZnO [20]. Although the proposed sensors showed excellent sensitivity and selectivity to $NO_2$, most of the reported sensors need to be operated at a high sensing temperature, which significantly reduces the lifespan of the sensors [21].

Thus, the demand for the development of room temperature and low-power consumption sensors is ever-growing, and the importance of appropriate technologies is significant as well. Among several techniques, UV-light illumination, incorporation of Nobel metals, and graphene-based composites are the most promising methods widely used for the development of room temperature sensors. For instance, Pargoletti *et al.* prepared graphene oxide–ZnO nano heterojunctions and studied its $NO_2$ sensing characteristics under UV light illumination [21]. The proposed sensor showed the $S_R$ of ~0.25 to 1 ppm of $NO_2$ at 25 °C. Wang et al. studied the synergistic effects of UV activation and surface oxygen vacancies on ZnO nanowires' $NO_2$ sensing performance at room temperature [22]. The proposed sensor was showed a wide range of detection limits ranging from 200 ppb to 1 ppm. The sensor's SR was found to be 1 toward 1 ppm of $NO_2$, signifying that the sensor is incapable of detecting a low concentration of $NO_2$ at room temperature (RT). However, the $S_R$ of the sensors is significantly low even under light illumination. Besides, the UV-assisted sensors have several technological disadvantages, such as size and harmful effects, including erythema, skin aging, coarse skin, pterygium, and long warm-up time. [23].

The incorporation of Nobel metal nanoparticles such as Au, Pt, Pd, and Ag into metal oxides matrix has been considered an effective method to improve the sensors' sensing characteristics [24–27]. The metal nanoparticles' high catalytic activity increases the number of oxygen vacancies on the surface of the sensor and significantly improved the sensitivity, selectivity, and reduced the operating temperature of the sensors. However, the metal nanoparticles are very expensive and not beneficial from a commercial viewpoint in the sensors' large-scale production for practical applications [21].

Graphene-based gas sensors have received considerable attention due to its outstanding charge carrier mobility, high conductivity, enhanced gas adsorption capacity, and chemically active defect sites [21,28]. However, the high response time and slow recovery time are significant drawbacks for the graphene-based sensors [29]. Recently, several dopants such as boron, nitrogen, and sulfur have been introduced into the graphitic structures to improve the graphene-based sensors' sensitivity, selectivity, and time-dependent sensing characteristics. For example, Lv *et al.* prepared a boron-doped graphene-based sensor and studied their $NO_2$ sensing characteristics at room temperature [30]. Wu *et al.* developed a chemically modified 3D sulfonated RGO hydrogel-based sensor and demonstrated its $NO_2$ sensing characteristics at ambient temperature [31]. The proposed sensor exhibits excellent sensitivity of 0.2 ppm with ultrafast response and recovery time of 12 s and 11 s. However, the sensor's selectivity is the major drawback as it also effectively detects $NH_3$ as low as 20 ppm with a response time of 16 s. Thus, the sensitive and selective detection of $NO_2$ in a ppb concentration at ambient temperature with fast response and recovery time remains challenging.

Indeed, the development of highly sensitive and selective room temperature sensor with rapid response and recovery time could be called an "innovation" for metal oxide-based gas sensors for environmental remedy applications. Herein, we developed an ultra-sensitive and selective room temperature $NO_2$ sensor by combining surface medication of ZnO with chemically functionalized carbon. Various characterization techniques were employed to demonstrate the successful formation of hybrid nanocomposites. The proposed sensor was prepared by a controlled hydrothermal method followed by carbonization at 850 °C under the Argon (Ar) atmosphere. The sensitivity of the proposed sensors was investigated in detail at different $NO_2$ concentrations and operating temperatures. The proposed NSC@ZNS sensor showed 1.5, 1.14, and 38.2 times enhanced $NO_2$ sensing response compared to NC@ZNS, SC@ZNS, and bare ZNS counterparts. Besides, the NSC@ZS sensor exhibits a LOD of 21 ppb at RT. The NSC@ZNS sensor showed ~31 times higher selectivity to $NO_2$ compared to other interfering gases.

## 2. Experimental section

### 2.1. Chemicals

Zinc acetylacetonate hydrate ($Zn(C_5H_7O_2)$. $XH_2O$), ethanolamine ($NH_2CH_2CH_2OH$), polyethylene glycol ($H(OCH_2CH_2)_n$. OH, urea ($NH_2CONH_2$), thiourea ($CH_4N_2S$), oxalic acid ($C_2H_2O_4$), sodium thiosulfate ($Na_2S_2O_3$) was purchased from Merck, South Korea, and used as received. The preparation method of hierarchical mesoporous ZNS, NC@ZNS, SC@ZNS and NSC@ZNS hybrid nanocomposites were illustrated in scheme 1.

### 2.2. Preparation of hierarchical mesoporous ZnO spheres (ZNS)

In a typical synthesis process, 2 mmol of zinc acetylacetonate hydrate (~0.52 g) was dissolved in 10 mL of ethanolamine under constant magnetic stirring followed by the addition of 10 mL of polyethylene glycol-400 and 2 mL of deionized water. The final reaction mixture was kept under ultrasonication for 15 min. Finally, the reaction mixture was transferred to the 40 mL Teflon-lined stainless-steel autoclave and heated to 200 °C at the rate of 10 °C/min in a programmable oven and maintained at that temperature for 24 h. After the hydrothermal reaction, the autoclave was oven cooled to room temperature. The precipitate was collected and washed several times with deionized water and ethanol to remove the residual impurities. Then, the obtained material was dried at 90 °C for 12 h.

### 2.3. Preparation of nitrogen-sulfur dual doped carbon@ ZnO spheres (NSC@ZNS)

In a typical synthesis procedure, 400 mg of thiourea was dissolved in 10 mL of deionized water. Then, 200 mg of as prepared ZNS was ultrasonically dispersed to the above solution. The resultant reaction mixture was kept under constant magnetic stirring at 90 °C for 12 h in a heating mantle. Subsequently, the reaction mixture was spread onto an evaporating dish forming a uniform solid mixture. Finally, the obtained powder was kept inside a quartz tube. Then, the quartz tube was evacuated using a vacuum pump for 10 min to remove the external moieties. The Ar gas was passed through a quartz tube for 15 min at a flow rate of 200 sccm to eliminate the atmospheric gases. Then, the quartz tube was heated to 850 °C at the heating rate of 5 °C/min and then annealed at that temperature for 3.5 h. The Ar gas was continued to flow through the quartz tube during the carbonization process at a flow rate of 200 sccm. After the annealing process, the crucible naturally cooled down to room temperature. The obtained material was ground to a fine powder for further analysis. The detailed synthesis procedures for the preparation of sulfur-doped carbon@ ZnO spheres (SC@ZNS) and nitrogen-doped carbon@ ZnO (NC@ZNS) hybrid nanocomposite were described in detail in the supplementary information.

## 3. Results and discussion

The field emission scanning electron micrograph (FESEM) of the as-

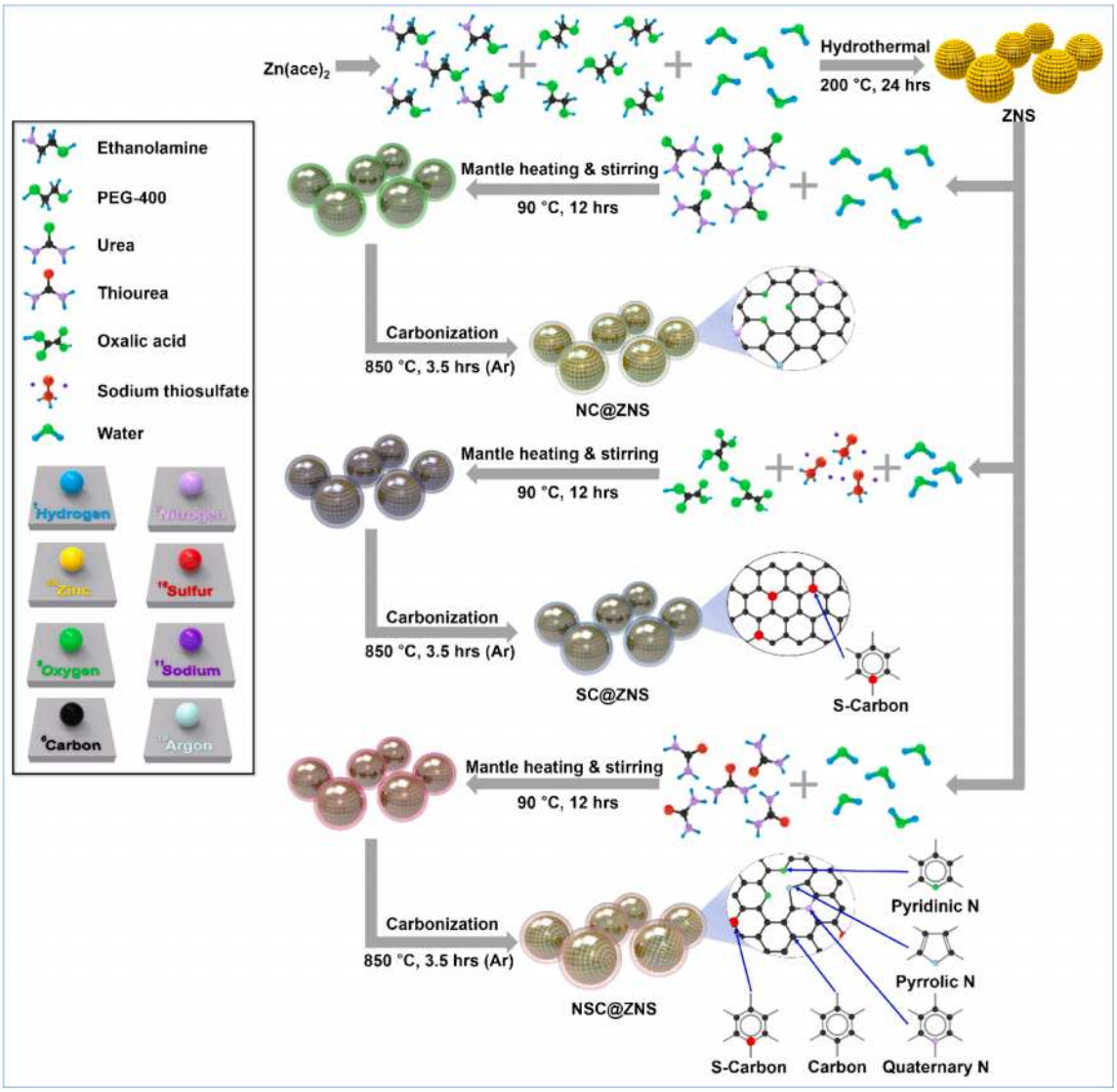


**Scheme 1.** Representation of the synthesis procedure of the hierarchical mesoporous ZNS, NC@ZNS, SC@ZNS, and NSC@ZNS hybrid nanocomposites.

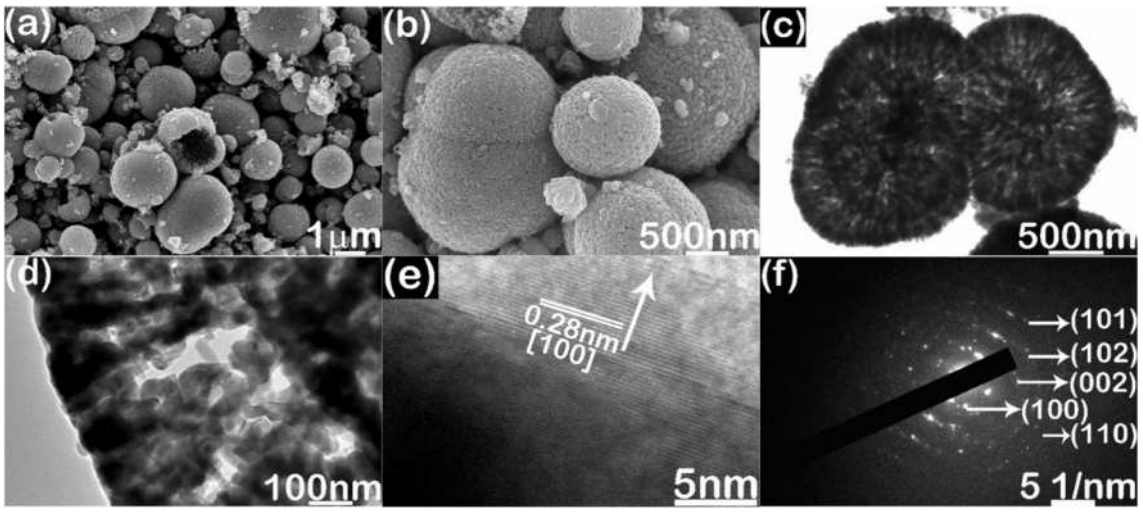


**Fig. 1.** Morphology of the as-prepared ZNS. (a, b) Scanning electron micrographs and (c, d) transmission electron micrographs of the as-prepared ZNS at different magnifications. (e) High-resolution transmission electron micrograph and (f) selected area electron diffraction pattern of the as-prepared ZNS.

prepared material shows several spheres with an average size of 1 μm (Fig. 1a). The higher-magnification image reveals that the as-prepared spheres are composed of several fine nanostructures with an average size of ~50 nm (Fig. 1b). Besides, some of the spheres are superimposed with each other and formed microspheres. The brighter and the darker spots in the transmission electron micrographs (TEM), demonstrating the hierarchical mesoporous nature of the obtained spheres (Fig. 1c, d). The high-resolution transmission electron micrograph (HRTEM) shows the lattice fringes with an average spacing of 0.28 nm corresponding to the [1 0 0] plane of the hexagonal wurtzite ZnO crystal structure (Fig. 1e) [32]. The selected area electron diffraction (SAED) pattern shows the diffraction rings attributed to the (1 0 0), (0 0 2), (1 0 2), and (1 0 1) plane of the wurtzite ZnO crystal structure (Fig. 1f) [33].

The FESEM image, Fig. 2a shows numerous as-prepared NCS@ZNS spheres with an average diameter of ~1 μm. Fig. 2b shows a closer view of the NCS@ZNS hybrid nanocomposite, demonstrating the uniform coating of carbon on the zinc oxide spheres. The TEM image of the as-prepared NCS@ZNS spheres concurred thoroughly with the FESEM analysis (Fig. 2c). The high magnified TEM image shows the core–shell structure of the as-prepared NCS@ZNS spheres (Fig. 2d). Fascinatingly, the closer view of these spheres under high magnifications shows several pores on the carbon layer. The electron-dense and electron depleted region are indicating the mesoporous nature of the as-synthesized product (Fig. 2f). The weak SAED pattern shows the diffraction plane attributed to the (0 0 2) and (1 0 1) plane of the carbon structure (Fig. 2g) [34]. The homogenous distribution of carbon, nitrogen, sulfur, zinc, and oxygen in the NSC@ZNS was confirmed by the electron dispersive spectra (EDS) elemental mapping (Fig. 2(h-m)). The inset of a panel in the EDS spectrum shows the atomic percentages of the elements in the NCS@ZNS hybrid nanocomposite. The proportions of the zinc, oxygen, carbon, nitrogen, and sulfur in the as-prepared material were ~51.9, 26.8, 15.6, 3.5 and 3.1, respectively. The morphological analysis of the as-prepared SC@ZNS and NC@ZNS hybrid nanocomposites are described in detail in the supplementary information (Figs. S1–S3).

The X-ray photoelectron spectra (XPS) analysis was performed to elucidate the composition of the as-prepared materials. The survey spectra show the photoelectron peaks from Zn, C, O, N, and S confirming the successful formation of the hybrid nanocomposites (Fig. 3a). Fig. 3b shows the XPS spectra of NC@ZNS, SC@ZNS and NSC@ZNS in the C1s region. The deconvoluted peaks at 284.6, 286.4, and 289. 5 eV can be

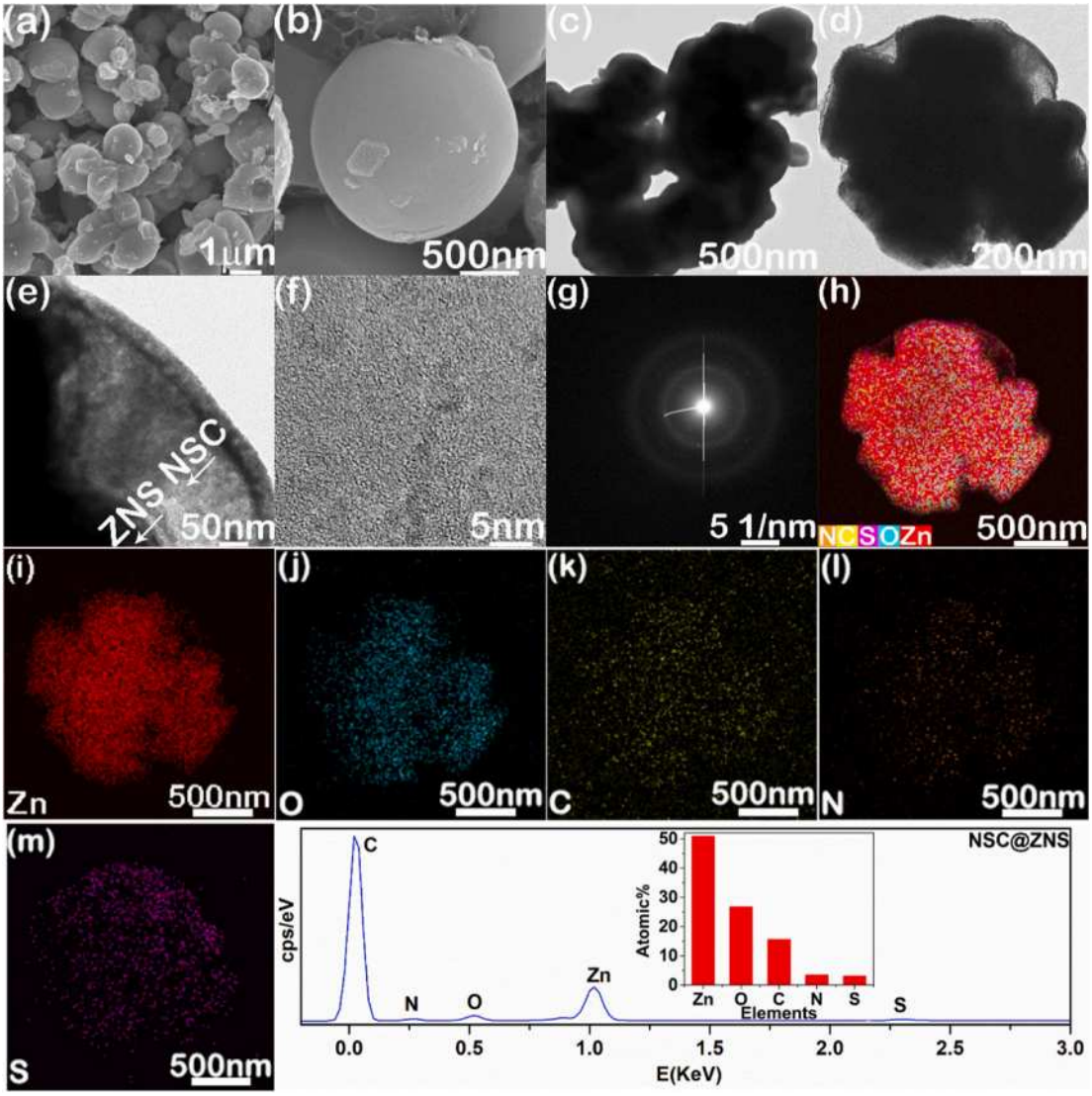


**Fig. 2.** Morphology of the as-prepared NSC@ZNS. (a-b) Scanning electron micrographs and (c-g) transmission electron micrographs of the as-prepared NSC@ZNS at different magnifications. (f) High-resolution transmission electron micrograph of the NSC@ZNS and (g) selected area electron diffraction pattern of the as-prepared NSC@ZNS. (h-m) Elemental mapping of the as-prepared NSC@ZNS hybrid nanocomposite. (n) Energy dispersive spectra of the as-prepared NSC@ZNS hybrid nanocomposite (inset shows the atomic percentage of Zn, O, C, N, and S in the as-prepared NSC@ZNS).

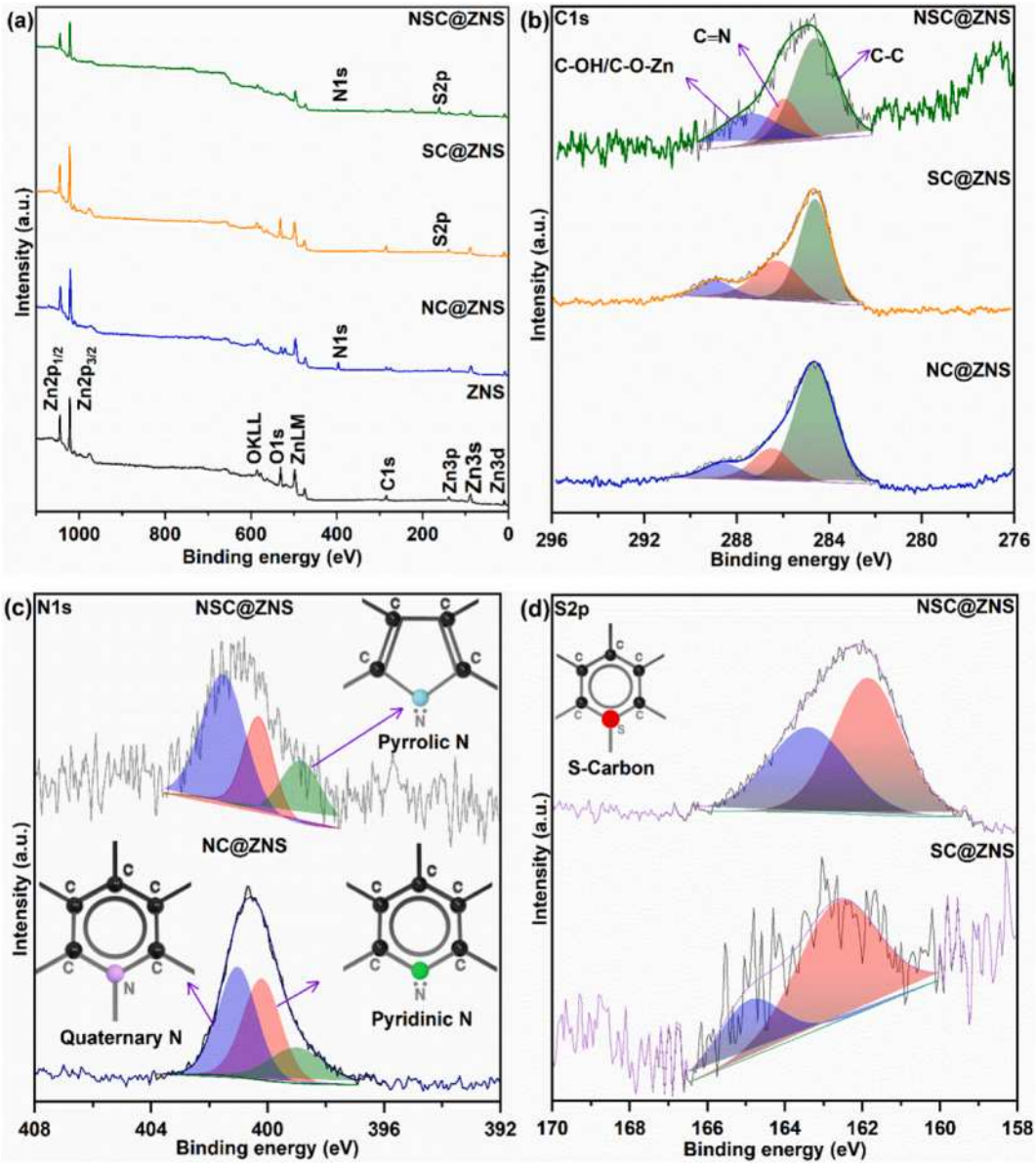


**Fig. 3.** X-ray photoelectron spectra of the as prepared hybrid nanocomposites. (a) The survey spectra of the as prepared ZNS, NC@ZNS, SC@ZNS and NSC@ZNS, (b) high-resolution carbon (C1s) and (c) nitrogen (N1s) spectra of the as-prepared NC@ZNS, SC@ZNS and NSC@ZNS. (d) High-resolution core-level sulfur (S2p) spectra of the as-prepared SC@ZNS and NSC@ZNS. Inset of a panel (c) and (d) shows the schematic illustration of different form of nitrogen-doped carbon and sulfur-doped carbon.

indexed to the C–C, C-N, and C-O-Zn/C-OH, respectively [35]. Fig. 3c shows the XPS spectra of NC@ZNS and NSC@ZNS in the N1s region. The hybrid nanocomposites show the photoelectron peaks at ~399, 400.3, and 401.5 eV are attributed to the different forms of nitrogen-doped in the carbon, such as pyrrolic nitrogen, pyridinic nitrogen, and quaternary nitrogen, respectively [21,28,36]. The deconvolution S2p spectrum of SC@ZNS and NSC@ZNS is shown in Fig. 3d. The photoelectron peaks at 162.9 and 163.9 eV, can be assigned to the $2p_{3/2}$ and $2p_{1/2}$ of the –C–S– covalent bond, respectively [37]. The atomic percentage of nitrogen in the NC@ZNS was ~23.7, while nitrogen-sulfur in the NSC@ZNS hybrid composite was ~5.11 and ~33.9, respectively. The atomic percentage of sulfur in the SC@ZNS nanocomposite was ~28.8. Table S1 show the atomic percentages of zinc, oxygen, carbon, nitrogen, and sulfur in the NC@ZNS, SC@ZNS and NSC@ZNS hybrid nanocomposites. The atomic percentages of the sulfur in the samples (SC@ZNS and NSC@ZNS) is higher than the N concentrations possibly due to the high tendency of sulfur to form metal sulfides during the carbonization process [38]. The CHNS analysis was carried out to measure the heteroatoms (S and N) bulk concentrations in the as-prepared materials. The presence of carbon, sulfur and nitrogen in the as-prepared nanocomposite was investigated by the CHNS elemental analysis. Table S2 shows the elemental concentrations presence in the samples measured by the XPS and CHNS analysis. The atomic percentage of carbon, nitrogen and sulfur was found to yield a very small standard deviation.

Fig. 4a(i, ii) shows the standard powder X-ray diffraction (XRD) pattern of the ZnO and carbon. The diffraction pattern at 2θ of 31.8°, 34.5°, 36.2°, 47.6°, 56.6°, 62.9°, 66.3°, 67.9°, 69.1°, 72.3° attributed to the (100), (002), (101), (102), (110), (103), (200), (112), (201), and (004) plane of the hexagonal wurtzite crystal structured ZnO with a *P63mc* space group (Fig. 4a(iii)) [39]. The calculated lattice parameters of the ZNS are a = b = 3.26 A° and c = 5.22 A° exactly matches the reported values of ZnO [39]. The XRD patterns of NC@ZNS, SC@ZNS and NSC@ZNS (Fig. 4a(iv-vi)) exhibits the similar diffraction patterns of ZNS (JCPDS No. 36–1451). Fig. S4 in the supplementary information

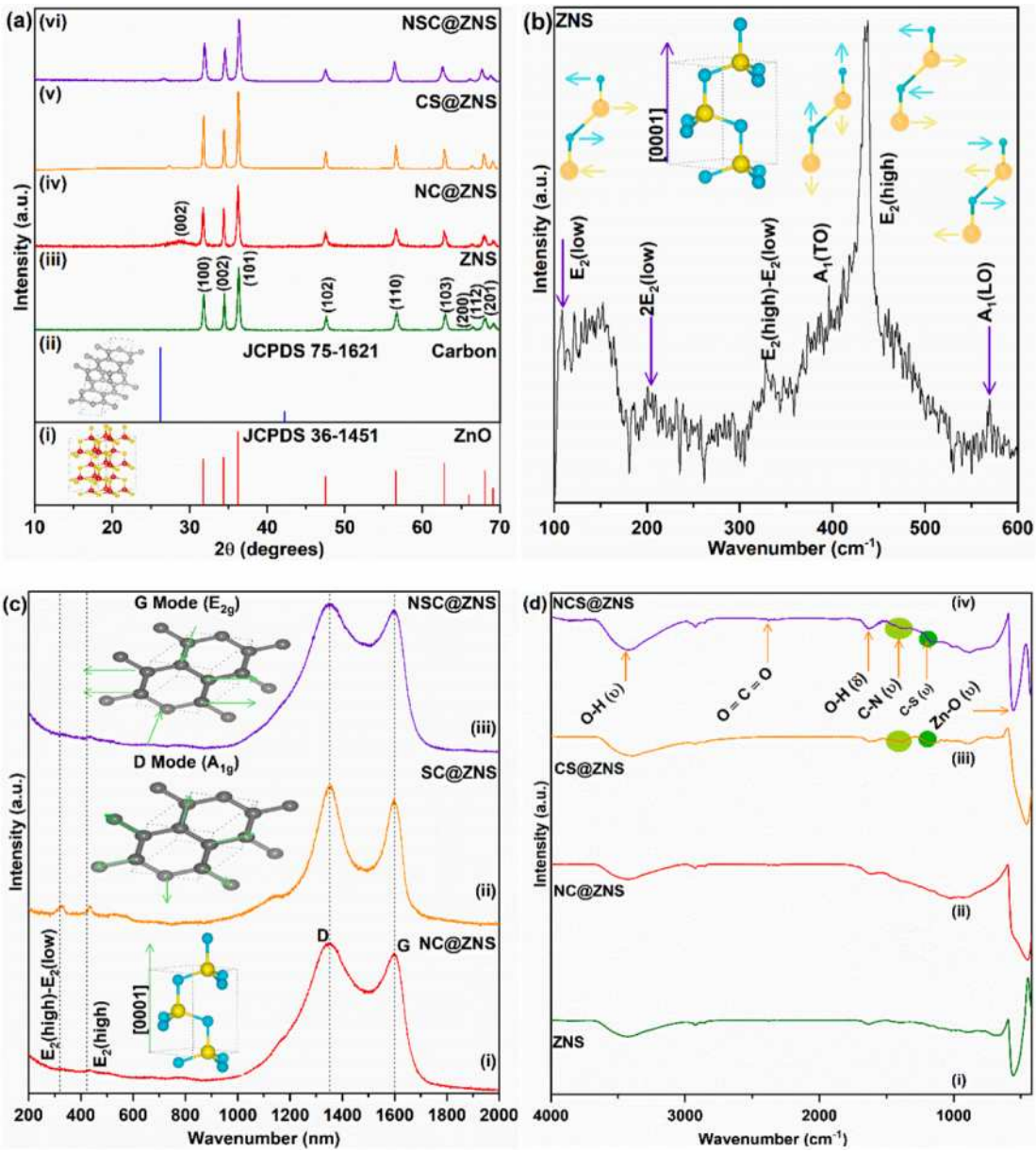


**Fig. 4.** (a) Powder X-ray diffraction pattern of the as-prepared ZNS, NC@ZNS, SC@ZNS and NCS@ZNS. Standard diffraction pattern of the (i) hexagonal wurtzite zinc oxide (JCPDS 36–1451) (inset shows the crystal structure of ZnO, yellow-Zn, and red-O) and (ii) carbon (JCPDS 75–1621) (inset shows the crystal structure of carbon). (iii-vi) diffraction pattern of the as-prepared ZNS, NC@ZNS, SC@ZNS and NSC@ZNS. (b) The micro-Raman spectrum of the as-prepared ZNS (inset crystal structure of ZnO, yellow-O, and blue-Zn). (c) The micro-Raman spectrum of the as-prepared NC@ZNS, SC@ZNS and NSC@ZNS (inset crystal structure of carbon). (d) Fourier transform infrared spectra of the as-prepared NC@ZNS, SC@ZNS and NSC@ZNS. (For interpretation of the references to colour in this figure legend, the reader is referred to the web version of this article.)

shows the enlarged view of the diffraction pattern of carbon in the NC@ZNS, and NSC@ZNS hybrid nanocomposites. The NC@ZNS shows the broad diffraction pattern at 26–28°, attributed to the (0 0 2) lattice plane of the disordered carbon structure (JCPDS No. 75–1621) [40]. The SC@ZNS nanocomposite shows the diffraction pattern at ~26.4° can be indexed to the (0 0 2) plane of the carbon structure. Besides, a carbon diffraction pattern was observed at 25–28° in the NSC@ZNS could be attributed to the formation of amorphous carbon on the ZNS structure. The interlayer spacing of carbon in the NC@ZNS, SC@ZNS and NSC@ZNS hybrid nanocomposite were calculated by the Bragg's equation. The interlayer spacing of carbon in NC@ZNS and NSC@ZNS is calculated to be 3.623 Å, 3.671 Å, and 3.662 Å, respectively. A higher $d_{(0\,0\,2)}$ interlayer spacing of carbon in the SC@ZNS and NSC@ZNS owing to the sulfur doping in the disordered carbon [41,42].

The Raman spectrum of the as-prepared ZNS shown in Fig. 4b. The phonon modes at ~108.5 and 199.1 $cm^{-1}$ corresponding to the $E_2$(low) and $2E_2$(low) primary vibrational modes of hexagonal wurtzite ZnO. The Raman band at 329.7 $cm^{-1}$ attributed to the fundamental second-order overtones ($E_2$high- $E_2$low) of ZnO [33,39]. The Raman band at 395.7 $cm^{-1}$ could be indexed to the first order vibrational ($A_1$ (TO)) optical phonon mode [43]. The Raman band at 437.1 $cm^{-1}$ attributed to the fundamental vibrational $E_2$ (high) mode. The Raman band positioned at 568.9 $cm^{-1}$ arises from the $A_1$ (LO) phonon mode associated with the presence of oxygen vacancies of hexagonal wurtzite crystal structured ZnO, respectively [33]. Fig. 4c shows the Raman spectra of as-prepared NC@ZNS, SC@ZNS and NSC@ZNS hybrid nanocomposites. The Raman bands at ~1350 $cm^{-1}$ and 1599 $cm^{-1}$ corresponding to the D and G band of the carbon [44]. The intensity ratio of D and G band provides

information on variations in the electronic conjugation state of the carbon. The $I_D/I_G$ values of NC@ZNS, SC@ZNS and NSC@ZNS were ~1.12, 1.17 and 1.19, respectively. The higher $I_D/I_G$ ratio of NSC@ZNS indicating the formation of a more defective carbon structure owing to the dual nitrogen and sulfur doping.

Fig. 4b shows the Fourier transform infrared (FTIR) spectra of the NC@ZNS, SC@ZNS and NSC@ZNS hybrid nanocomposites. The FTIR spectra shows the adsorption bands from ZnO, carbon, nitrogen, and sulfur. The absorption bands at 425 and 524 $cm^{-1}$ corresponding to the fundamental transverse and longitudinal optical stretching vibrations of ZnO [45]. The broad absorption band at 3429 $cm^{-1}$ corresponding to the stretching vibration of bonded and non-bonded –OH groups. The peaks at 1610 and 1461 $cm^{-1}$ due to the stretching vibrations of C = N and C–N, respectively [46]. The FTIR peaks in the range of 1000–1400 $cm^{-1}$ attributed to the stretching vibrations of C–O, C–S, and C–H, respectively [47].

Fig. S5 shows the thermal gravimetric (TG) profile of the as-prepared NC@ZNS, SC@ZNS, and NSC@ZNS hybrid nanocomposite. The TG measurements were carried out under the air atmosphere from room temperature to 900 °C at a heating rate of 10 °C/min. The weight loss up to ~150 °C attributed to the removal of bound water molecules from the materials' surface. The weight loss from 250 °C to 700 °C resulting from the reduction of oxygen-containing functional groups and the decomposition of the carbon in the hybrid nanocomposites. Based on the TGA analysis, the estimated weight ratio of carbon in the NC@ZNS, SC@ZNS, and NSC@ZNS hybrid nanocomposite was ~19, 16, and 21%, respectively.

Fig. S6 shows the nitrogen adsorption/desorption Barret– Joyner–Halenda (BJH) isotherm of the as-prepared ZNS, NC@ZNS, SC@ZNS and NSC@ZNS hybrid nanocomposites. All the materials exhibit type-IV isotherms, indicating the presence of micro- and mesoporous in the as-prepared materials [21,28]. The Brunauer– Emmett–Teller (BET) surface area of the ZNS, NC@ZNS, SC@ZNS and NSC@ZNS calculated as 32 $m^2.g^{-1}$, 68 $m^2.g^{-1}$, 74 $m^2.g^{-1}$ and 76 $m^2.g^{-1}$, respectively. The cumulative pore volume of ZNS, NC@ZNS, SC@ZNS and NSC@ZNS hybrid nanocomposite is estimated to be ~0.27, 0.18, 0.22 and ~0.12 $cm^3.g^{-1}$,

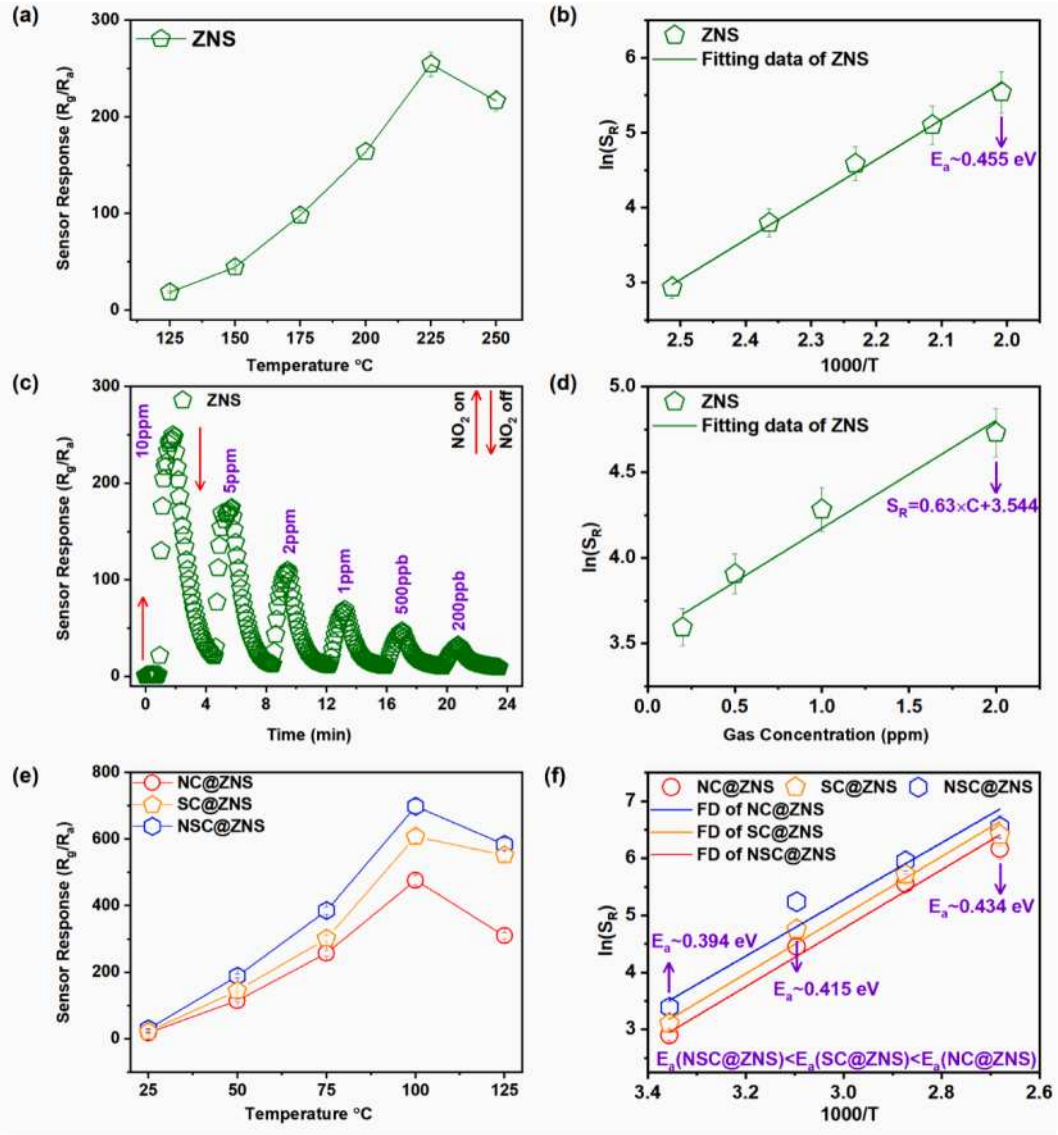


**Fig. 5.** Gas sensing characteristics of the fabricated sensors based on ZNS, NC@ZNS, SC@ZNS and NSC@ZNS hybrid nanocomposites. (a) Temperature-dependent sensing response of the ZNS sensor to 10 ppm of $NO_2$. (b) Arrhenius plot of the sensor response. (c) Dynamic sensing response of the ZNS sensor at 225 °C toward different concentrations of $NO_2$. (d) Linear plot representing the sensor response as a function of $NO_2$ concentrations at 225 °C. (e) Temperature-dependent sensing response of the NC@ZNS, SC@ZNS and NSC@ZNS hybrid nanocomposites sensor to 10 ppm of $NO_2$. (f) Arrhenius plot of the sensor response. [FD: Fitting data, Gc: Gas concentration]

respectively, and the corresponding pore size of the materials are ~8.7, 4.3, 5.2, 3.1 nm, respectively. The inset of Fig. S6 shows the pore size distribution plots of ZNS, NC@ZNS, SC@ZNS and NSC@ZNS hybrid nanocomposite. All the materials exhibit the pores in the range of 2–100 nm, suggesting the mesoporous- and microporous nature of the materials [21,28].

The details of the sensor fabrication and $NO_2$ sensing characteristics analysis have been described in the supplementary information [21,28]. The $S_R$ of the sensor is defined as the ratio of the sensor resistance in the presence of $NO_2$ and in the presence of air [48,49]. Response time ($\Gamma_{RES}$) of the sensor is defined as the time required for the sensor to reach 90% of its resistance in the presence of gas and the recovery ($\Gamma_{REC}$) time of the sensor is defined as time taken by the sensor to reach 10% of its original resistance in the presence of dry air [50]. The temperature-dependent sensing characteristics of the ZNS, NC@ZNS, SC@ZNS and NSC@ZNS sensors were carried out to identify the optimum operating temperature for the sensors. Fig. 5a shows the $S_R$ of the ZNS sensor at different operating temperatures to 10 ppm of $NO_2$. The $S_R$ of the sensor was found to be increased with increasing operating temperature. The $S_R$ of the ZNS sensor at 100, 125, 150, 175, 200, 225, 250 °C was found to be ~18.3, 43.9, 97.5, 163.8, 253.2, and 215.2, respectively. The activation energy (Ea) of the sensor is an important parameter that determined the sensitivity of the sensor. Therefore, the Ea of the ZNS sensor was calculated by the corresponding Arrhenius plot of the $S_R$. The Ea of the sensor was calculated using the Arrhenius equation [21].

$$S_R = S_0 \exp\left(\frac{E_a}{2K_B T}\right) \quad (1)$$

where, Ea, $K_B$, T, $S_0$, and $S_R$ are the activation energy, Boltzmann constant, sensing temperature, sensing response and constant, respectively. Fig. 5b shows the linear dependence of the ln($S_R$)of *vs.* the reverse of the sensing temperature (1/T). The calculated Ea of the ZNS sensor was found to be ~0.455 eV.

The maximum sensitivity of the ZNS was investigated at 225 °C to different $NO_2$ concentrations ranging from 10 ppm to 200 ppb (Fig. 5c). The $S_R$ of the ZNS sensor to 10, 5, 2, 1, 0.5, and 0.2 ppm was ~260.1, 185.3, 119.8, 81.3, 58.8, 43.9, respectively. The $S_R$ of the ZNS sensor as a function of $NO_2$ concentrations can be described using the following empirical equation [21].

$$S_R = 1 + \alpha G_C^{\beta} \quad (2)$$

where $S_R$, $G_C$, α, and β are the sensing response, gas concentration, constant, respectively. The $S_R$ of the ZNS sensor to 200 ppb-2 ppm range shows a strong linear relation. Such a relationship can be represented as below.

$$S_R = 0.63 \times G_C + 3.544 \quad (3)$$

The theoretical limit of detection (LOD) of the ZNS sensor can be obtained when the $S_R$ is three times higher than the noise of the signal [51]. The following equation was used to calculate the LOD of the ZNS sensor [21].

$$S_R = 3 \times \frac{RMS_{noise}}{Slope} \quad (4)$$

The LOD of the sensor was calculated from the slope of the linear portion and RMS noise at the baseline of the sensing response [52]. The LOD of the ZNS sensor was found to be ~30 ppb at 225 °C.

Fig. 5e shows the temperature dependent sensing characteristics of the fabricated sensors based on NC@ZNS, SC@ZNS and NSC@ZNS hybrids at different operating temperatures. The $S_R$ of the NC@ZNS, SC@ZNS and NSC@ZNS sensors at 25, 50, 75, 100, 125 °C were ~18.1, 115.2, 257.8, 476.9, 310.2, 22.3, 145.21, 302.12, 608.27, 552.32 and 29.7, 189.1, 385.4, 699.2, and 584.2, respectively. All three sensors exhibited enhanced sensitivity and showed the maximum $S_R$ at 100 °C. The $S_R$ of the NSC@ZNS sensor is ~1.5 and 1.15 times higher than that of NC@ZNS and SC@ZNS sensors. Most importantly, all three sensors showed a completely reversible response to $NO_2$ at room temperature. The Ea of the sensors was calculated by the Arrhenius plots of the ln($S_R$) *vs.* reverse of the sensing temperature (1/T), as described in the method mentioned above. The calculated Ea of the NCS@ZNS, SC@ZNS and NC@ZNS was ~0.394, 0.415 and 0.434 eV, respectively (Fig. 5f). The lower Ea of the NCS@ZNS sensor indicating the higher sensing performance of the material.

Fig. 6 shows the dynamic $S_R$ of the fabricated sensors based on NC@ZNS, SC@ZNS and NSC@ZNS to different concentrations of $NO_2$ ranging from 10 ppm to 200 ppb at 25, 50, and 100 °C. The $S_R$ of the sensors increases with increasing $NO_2$ concentrations. The $S_R$ of NC@ZNS, SC@ZNS sensors at 25 °C were found to be ~19.6, 17.4, 14.8, 11.8, 8.9, and 24.56, 20.24, 18.16, 15.11 and 11.14 to 10, 5, 2, 1, and 0.5 ppm of $NO_2$, respectively. In comparison, the NSC@ZNS sensor shows a response of ~31.2, 30.1, 24.6, 21.1, and 14.32 at the same concentration (Fig. 6a). The LOD of the NC@ZNS, SC@ZNS and NSC@ZNS sensors were ~28 ppb, 25 ppb and 21 ppb, respectively. The $S_R$ of the NC@ZNS, SC@ZNS and NSC@ZNS sensors at 50 °C to 10, 5, 2, 1, 0.5, 0.2 ppm of $NO_2$ was ~118.2, 104.3, 99.1, 79.2, 63.1, 36, 137.69, 128.27, 109.02, 87.51, 73.18, 46.12 and 196.2, 179.2, 154.8, 119.4, 95.5, and 58.3, respectively (Fig. 6c). The $S_R$ of the NC@ZNS, SC@ZNS and NSC@ZNS sensors at 100 °C to 10, 5, 2, 1, 0.5, 0.2 ppm of $NO_2$ were ~505.2, 369.2, 264.3, 180.2, 150.2, 121, 593.61, 461.65, 315.03, 224.67, 157.14, 128.46 and 730.4, 553.5, 347.2, 230.6, 172.8, and 129.6, respectively (Fig. 6e). With increasing operating temperature, the sensitivity of the sensors increased. Besides, the response time and recovery time of the sensors decreased due to the thermal acceleration of gas kinetic reactions. As evident from the sensing analysis, the NC@ZNS, SC@ZNS and NSC@ZNS hybrid nanocomposite exhibit not only an enhanced sensing response but also a wide range of detection limits. At all temperatures, the NSC@ZNS hybrid nanocomposite sensor showed ~1.43 and 1.23 times higher sensing response than that of NC@ZNS and SC@ZNS sensors. The following equations can describe the linear relationship between the sensing response (ln(SR)) of NC@ZNS, SC@ZNS and NSC@ZNS sensors as a function of gas concentration at different operating temperatures (Fig. 6 (b, d, and f)).

$$NC@ZNS - S_{R@25} = 0.13 \times G_C + 2.23 \quad (5)$$

$$SC@ZNS - S_{R@25} = 0.16 \times G_C + 2.37 \quad (6)$$

$$NSC@ZNS - S_{R@25} = 0.16 \times G_C + 2.55 \quad (7)$$

$$NC@ZNS - S_{R@50} = 0.23 \times G_C + 3.52 \quad (8)$$

$$SC@ZNS - S_{R@50} = 0.191 \times G_C + 3.987 \quad (9)$$

$$NSC@ZNS - S_{R@50} = 0.22 \times G_C + 3.98 \quad (10)$$

$$NC@ZNS - S_{R@100} = 0.21 \times G_C + 4.54 \quad (11)$$

$$SC@ZNS - S_{R@100} = 0.209 \times G_C + 5.11 \quad (12)$$

$$NSC@ZNS - S_{R@100} = 0.25 \times G_C + 4.61 \quad (13)$$

The repeatability of the fabricated sensors based on NC@ZNS, SC@ZNS and NSC@ZNS hybrid nanocomposites during two continuous cycles was investigated at 75 °C to different concentrations of $NO_2$ ranging from 10 ppm to 1 ppm. The $S_R$ of the NC@ZNS, SC@ZNS and NSC@ZNS sensors decreased with decreasing the $NO_2$ concentrations and recover back to their previous response value with increasing the $NO_2$ concentration (Fig. 7a). Besides, the stability of the fabricated gas sensors at ~25 °C was examined to 500 ppb of $NO_2$ (Fig. 7b). The $S_R$ of the NC@ZNS, SC@ZNS and NSC@ZNS sensors was found to be in the range of ~8.4 ± 0.88, 11.32 ± 0.47 and 13.4 ± 0.96 and respectively, for 5 repetitive cycles, indicating the stable response and recovery

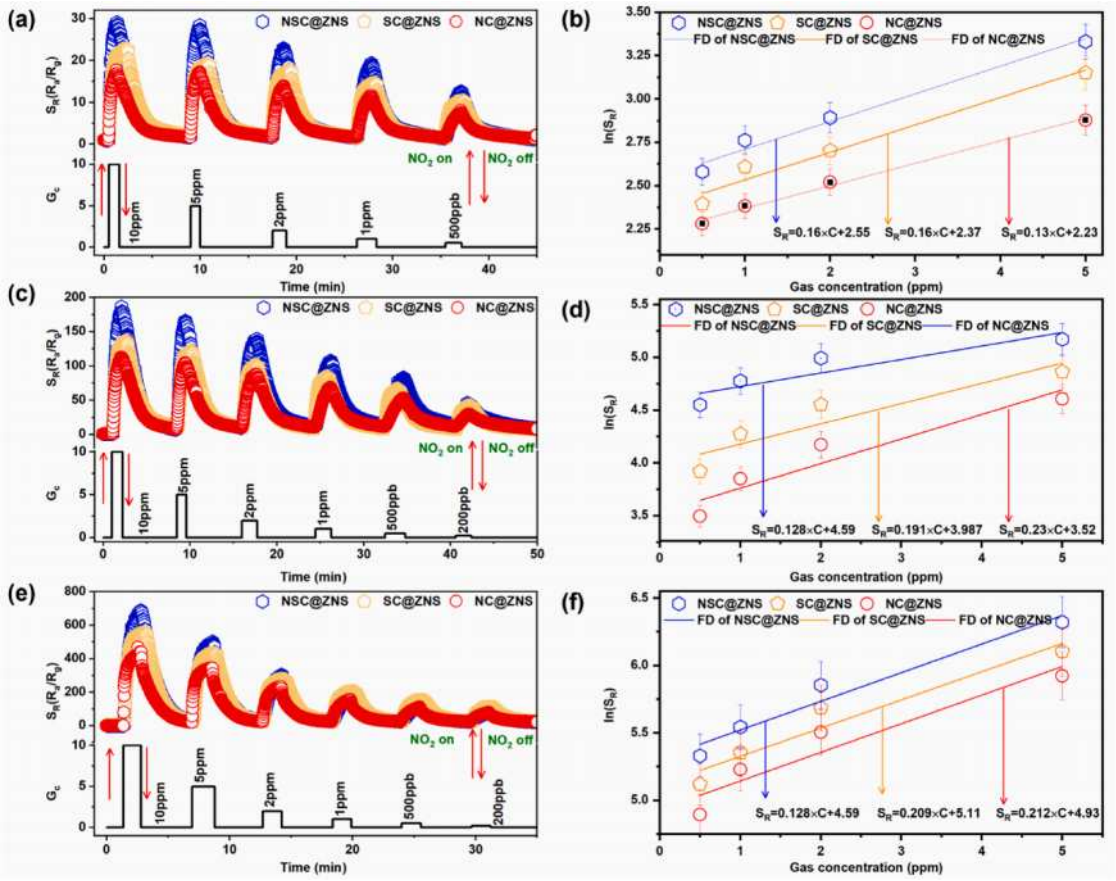


**Fig. 6.** Gas sensing characteristics of the fabricated sensors based on NC@ZNS, SC@ZNS and NSC@ZNS hybrid nanocomposites. (a, c, and e) Dynamic sensing response of the sensors at 25, 50, and 100 °C toward different concentrations of $NO_2$. (b, d, and f) Linear plot representing the sensor response as a function of $NO_2$ concentrations at 25, 50, and 100 °C. [FD: Fitting data, Gc: Gas concentration]

characteristics of the proposed sensors. Long-term stability is one of the most crucial for a practical application of the sensors. Therefore, the sensing response of the NSC@ZNS sensor was investigated for 35 days. Fig. S7 shows the NSC@ZNS sensor $NO_2$ response to 10 ppm of $NO_2$ as a function of measurement days. The sensing transients of the sensor after continuous measurement cycles for 5 weeks at specific time intervals showed a response without any significant changes. The obtained sensing results revealed the impressive long-term stability of the sensor based on NSC@ZNS hybrid nanocomposite. The exceptional response and recovery $NO_2$ sensing characteristics of the sensors are owing to the excellent structural integrity, robustness, and electrical behavior of the sensing materials.

The $\Gamma_{RES}$ of the sensors based on NC@ZNS, SC@ZNS and NSC@ZNS to 500 ppb of $NO_2$ at 25 °C was found to be ~76 s, 74 s, 88 s, respectively, while the $\Gamma_{REC}$ of the sensors were ~340 s, 332 s and 305 s, respectively (Figs. S8, S9). The $\Delta E\Gamma_{RES}$ and recovery $\Delta E\Gamma_{REC}$ times of the NC@ZNS, SC@ZNS and NSC@ZNS sensors to 1 ppm $NO_2$ was compared as a function of operating temperature. Fig. S10 shows the linear dependence of the logarithm of time constants (ln(t)) *vs.* the reverse of the sensing temperature. The potential barrier heights of the sensors were calculated from the slope of the linear portion of the plot using the thermal activation function. The $\Delta E\Gamma_{RES}$ barrier heights of the NC@ZNS, SC@ZNS and NSC@ZNS sensors were found to be 75, 71 and 69 meV, respectively. While $\Delta E\Gamma_{REC}$ of the NC@ZNS, SC@ZNS and NSC@ZNS sensors were ~41, 42 and 44 meV, respectively. The smaller barrier heights were signifying that the NSC@ZNS sensor surface is most favorable for the adsorption-oxidation-desorption gas kinetic reaction [53,54].

The selectivity of the NSC@ZNS sensor was tested at 25 °C to 10 ppm of $H_2S$, $NH_3$, CO, $H_2$, $CH_4$, and $NO_2$. As shown in Fig. 8, the sensor showed a higher response to $NO_2$ compared to other interfering gases. The response of the sensor to $H_2S$, $NH_3$, $CH_4$, CO, $H_2$, and $NO_2$ was ~1.39, 1.3, 1.11, 1.09, 1.03, and 29.98, respectively. The sensing response ratio of $H_2S$, $NH_3$, $CH_4$, CO, $H_2$ to $NO_2$ was ~0.046, 0.043, 0.037, 0.036, 0.034, indicating the excellent $NO_2$ selectivity of the fabricated sensor. Besides, the sensing response of the NSC@ZNS sensor does not significantly affect to the relative humidity in the range of 20–90%, indicating that the environment humidity does not affect the sensor (Fig. S11).

## 4. Gas sensing mechanism

Firstly, we would like to describe the general $NO_2$ sensing mechanism of pristine ZnO nanostructure. At elevated operating temperature, typically above 200 °C, the surface adsorbed oxygen converts into the oxygen radicals, thereby generating an electron-depleted region. The typical reactions can be expressed by the following equations 14–16 [29].

$$O2(g) \rightarrow O2(ads) \quad (14)$$

$$O2(ads) + e- \rightarrow O2–(ads) \quad (15)$$

$$O2–(ads) + e- \rightarrow 2O–(ads) \quad (16)$$

Upon exposure to $NO_2$, gas kinetic reactions are commenced, whereby the $NO_2$ molecule traps the electrons from sensing material, thus increases the sensor resistance. The $NO_2$ molecules can interact with the sensor surface in two ways, (i) direct extraction of electrons from the ZnO conduction band and/or (ii) indirectly from the oxygen

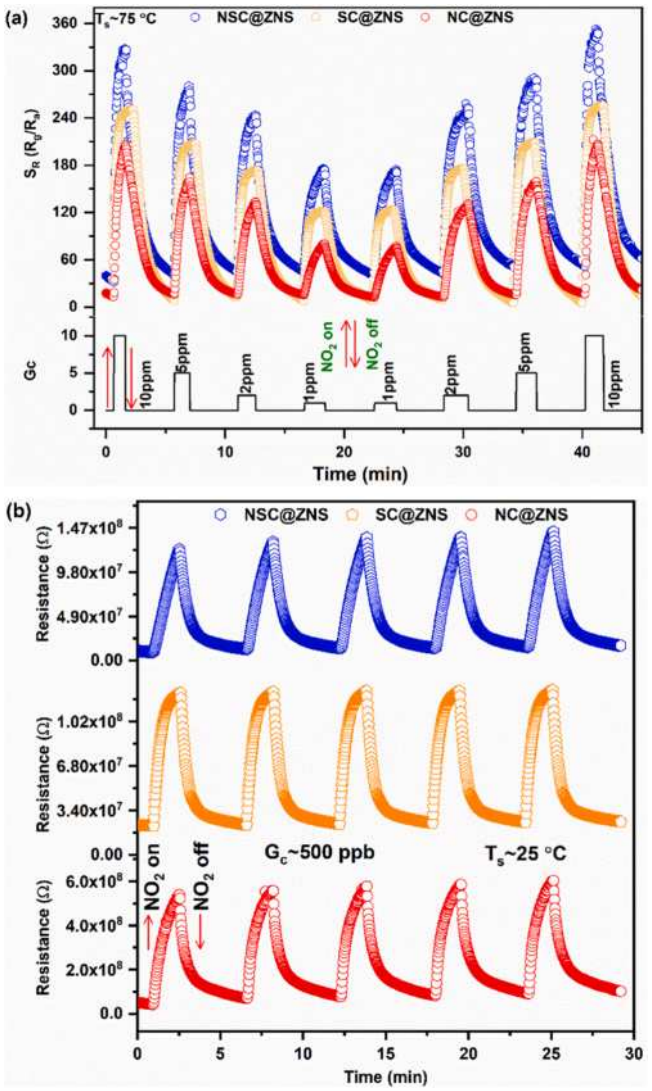


**Fig. 7.** Gas sensing characteristics of the fabricated sensors based on NC@ZNS, SC@ZNS and NSC@ZNS hybrid nanocomposites. Dynamic sensing response of the sensors at 75 °C toward different concentrations of $NO_2$. Repeatability of the fabricated sensors at 25 °C to 500 ppb of $NO_2$ for 5 cycles.

radicals chemisorbed on the ZnO surface. The specific reactions are described as follows [55].

$$2NO2(g) \rightarrow 2NO2(ads) \quad (17)$$

$$NO2(ads) + e\text{-} \leftrightarrow NO2\text{–}(ads) \quad (18)$$

$$NO2(ads) + e\text{-} \leftrightarrow NO(g) + O\text{-}(ads) \quad (19)$$

$$NO2(ads) + O2\text{–}(ads) + 2e\text{-} \leftrightarrow NO2\text{–}(ads) + 2O\text{–}(ads) \quad (20)$$

$$NO(g) + 1/2O2 \rightarrow NO2(g) \quad (21)$$

The ZNS sensor showed enhanced sensitivity as low as 200 ppb with the sensor response of 44 at 225 °C. The LOD of the ZNS sensor was found to be ~30 ppb at 225 °C. However, the ZNS sensor could not be able to detect $NO_2$ below 100 °C. This could be explained based on the following lines. When the sensor operates at a high temperature (≥200 °C), the oxygen radicals generated on the sensor surface, where electrons reduce the $O_2$ molecules, but it is challenging to produce the significant volume oxygen radicals at ambient temperatures. Therefore, the assistance of a catalyst for oxygen reduction is necessary for the development of room temperature sensors.

In this work, the room temperature $NO_2$ sensing is achieved by the formation of nitrogen-sulfur dual doped carbon on the ZnO spheres. The incorporation of NSC on the ZNS efficiently improved the $NO_2$ sensing response at ambient temperatures. The enhanced $NO_2$ sensing characteristics of the NCS@ZNS sensor could be attributed to (i) high catalytic activity stimulated by sulfur and nitrogen doping, (ii) chemical sensitization by the sulfur and nitrogen in the carbon matrix, (iii) electric effects triggered by the heterojunction between NSC and ZNS, (iv) Large surface area and porous structure of the sensing material. The impact of all these factors on the enhanced sensitivity of the NSC@ZNS sensor is discussed one by one in the following sections.

The catalytic effect of nitrogen-sulfur-doped carbon has been widely reported in several oxygen reduction reactions (ORR) studies [56–59]. The doping of nitrogen and sulfur redistribute the charge density of adjacent C atoms on the carbon matrix, owing to the substantial electronegativity variations between C/N and C/S atoms ($\chi N = 3.04$, $\chi S = 2.58$ and $\chi C = 2.55$) [59]. Thus, the carbon atoms nearer to the nitrogen and sulfur atoms possess positively charged on the carbon matrix. This localized electrostatic potential acts as energetic sites and readily available for facilitating the chemisorption of oxygen. The active nitrogen-sulfur sites play as an electron donor and promote the formation of oxygen radicals. The formation of a large density of oxygen radicals on the sensor surface can be explained based on the XPS spectra analysis.

Fig. 9a shows the O1s XPS core-level spectra of the as-prepared ZNS, NC@ZNS, SC@ZNS and NSC@ZNS hybrid nanocomposite. The O1s spectra deconvoluted into three peaks depending on its oxidation state. The peaks at 529.3 eV attributed to metal–oxygen bonds in ZnO. The other peaks located at 531.4, and 532.7 eV can be assigned to the $O^{2-}$ ions in surface adsorbed oxygen and chemisorbed oxygen, respectively [60]. The relative peak percentage of the chemisorbed oxygen on the ZNS, NC@ZNS, SC@ZNS and NSC@ZNS were found to be ~12, 26, 31 and 38, respectively. The higher chemisorbed oxygen on the NSC@ZNS hybrids could be attributed to the excellent oxygen reduction catalytic nature of nitrogen-sulfur doped carbon. The generated oxygen radicals are then diffused into the surface vacancies of ZnO by the chemical sensitization effect. Thus, more trapped electrons are produced, leading to an increase in the sensor resistance, subsequently an enhancement in the sensitivity of the sensor. The dual doping of nitrogen and sulfur in carbon produces more defective active sites for the oxygen reduction reactions compared to that of pristine nitrogen-doped carbon. This justifies why the NSC@ZNS sensor exhibited higher sensitivity than that of NC@ZNS, SC@ZNS and ZNS sensors. Besides, the sensitivity of the NSC@ZNS sensor enhanced by the strong chemical and electronic interaction between the NSC and ZNS. Fig. 9b shows the high-resolution core-level spectra of ZNS, NC@ZNS, SC@ZNS and NSC@ZNS in the Zn 2p region. The photoelectron peaks at 1022.4 and 1045.2 eV, attributed to the $2p_{3/2}$ and $2p_{1/2}$ doublet of $Zn^{2+}$, respectively [61]. The photoelectron peaks of NC@ZNS, SC@ZNS and NSC@ZNS shift 0.5 eV to the higher binding energy compared to that of the pristine ZNS, indicating the strong chemical and electronic interaction between zinc oxide and doped carbon.

Further, the exceptional $NO_2$ sensing performance of the NSC@ZNS sensor could be attributed to the chemical modification of carbon with nitrogen and sulfur. The nitrogen and sulfur are more electronegative than the carbon and tend to pull some electrons from the neighboring carbon atoms by the inductive effect, thus, increase the number of holes in the modified carbon. $NO_2$ is an electron extracting gas and can quickly adsorb on the electron-rich sites such as lone pairs of electrons of S and N in the carbon matrix. After $NO_2$ adsorption, the electron-withdrawing ability of the sulfur group was increased and consequently enhanced the sensitivity of the sensor. The $SO_3^-$ group in the NSC@ZNS and SC@ZNS has a more-significant number of lone-pair electrons compared to that of NC@ZNS hybrid nanocomposite. Thus, the NSC@ZNS, SC@ZNS sensors have a significantly higher capability to adsorb $NO_2$ than the NC@ZNS sensor. Dai et al. theoretically demonstrated that the

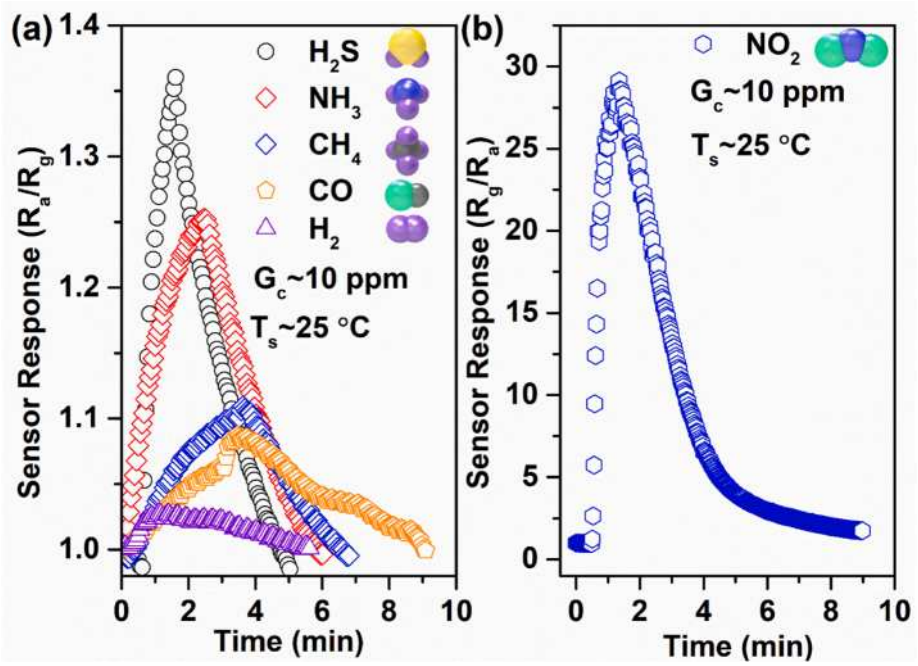


**Fig. 8.** Selectivity of the fabricated sensor based on NSC@ZNS hybrid nanocomposite at 25 °C. (a) Sensing response of the NSC@ZNS sensor to 10 ppm of $H_2S$, $NH_3$, $CH_4$, CO and $H_2$. (b) $NO_2$ sensing response of the NSC@ZNS sensor to 10 ppm of $NO_2$.

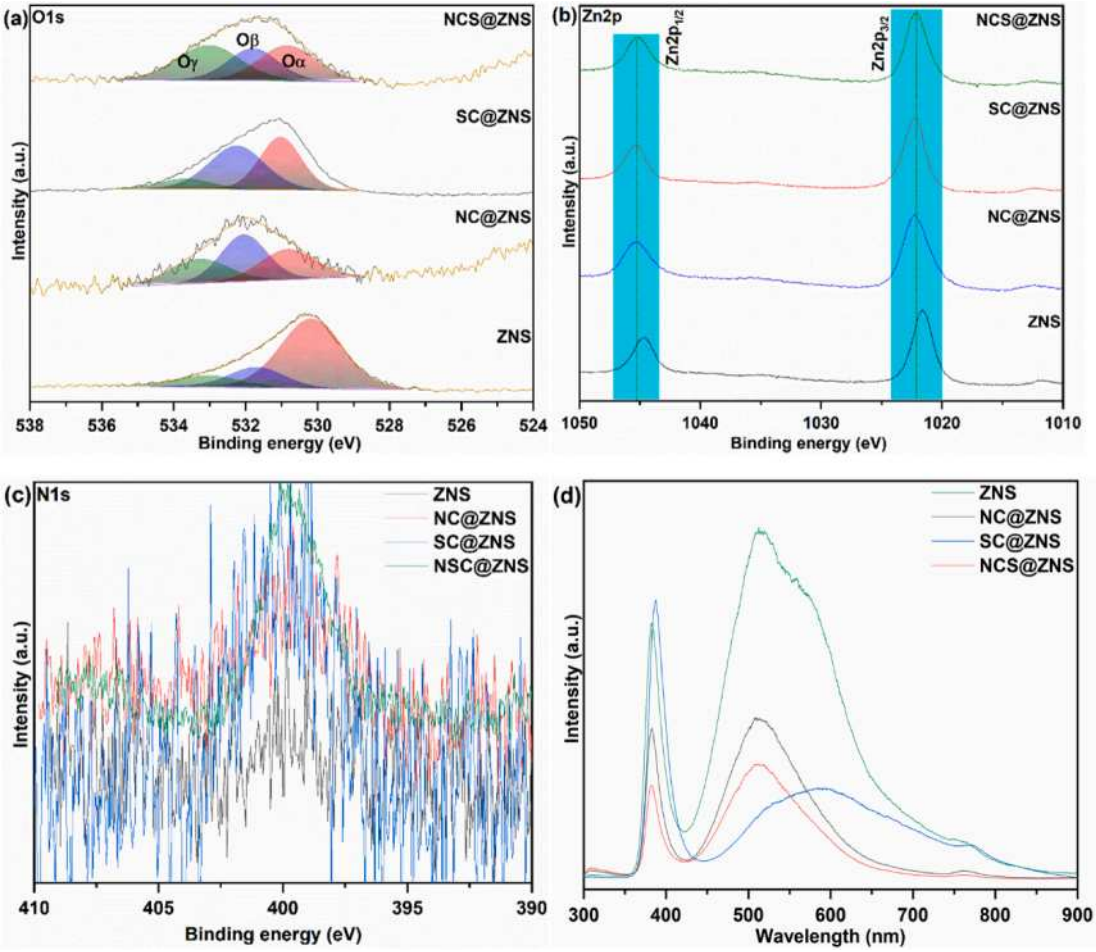


**Fig. 9.** (a) Oxygen (O1s) spectra of the as-prepared ZNS, NC@ZNS, SC@ZNS and NCS@ZNS hybrid nanocomposites. (b) Zinc (Zn2p) spectra of the ZNS, NC@ZNS, SC@ZNS and NCS@ZNS hybrid nanocomposites. (c) N1s spectra of the fabricated sensors based on ZNS, NC@ZNS, SC@ZNS and NCS@ZNS hybrid nanocomposites after exposure to 50 ppm of $NO_2$ at 50 °C. (d) Photoluminescence spectra of the ZNS, NC@ZNS, SC@ZNS and NCS@ZNS hybrid nanocomposites.

$NO_2$ molecules could chemically bind with S-active sites in the carbon matrix compared to that of pristine N-active sites in the carbon [62].

The active participation of the dual doped NSC@ZNS sensor in $NO_2$ chemisorption can be explained based on the XPS analysis. Fig. 9c shows the N1s spectra of the ZNS, NC@ZNS, SC@ZNS and NCS@ZNS sensors after exposure to 50 ppm of $NO_2$ at 50 °C. The relative N1s peaks percentage of the ZNS, NC@ZNS, SC@ZNS and NCS@ZNS sensors before and after $NO_2$ sensing were found to be ~0, 23.7, 0.72 and 5.1 and 0.54, 29.21, 22.32 and 27.77, respectively. The small peak observed at 405–410 eV could be attributed to the different forms of chemisorbed $NO_2$ species on the surface of the sensors. The presence of $NO_2^-$ and $NO_3^-$ is attributed to the reduction of $NO_2$ by oxygen radicals on the surface of the sensors [63].

The enhanced sensitivity of the NSC@ZNS sensor is not only due to the catalytic effect of nitrogen and sulfur-doped carbon, but also the synergy between the NSC and ZNS. The heterojunction between the NSC and ZNS increased the sensitivity of the sensor. The interface effect between the NSC and ZNS can be explained based on the photoluminescence (PL) spectra analysis. Fig. 9d shows the PL spectra of the as-prepared ZNS, NC@ZNS, SC@ZNS and NSC@ZNS hybrids. The NSC@ZNS, SC@ZNS nanocomposite showed much lower intensity compared to that of NC@ZNS and ZNS, indicating that NSC and SC acting as a better electron acceptor compared to that of NC, thus, reducing the PL intensity of ZNS. The heterojunctions between NSC and ZNS behave as electron migration routes that enhance the sensitivity of the sensor. Besides, the enhanced sensitivity of the sensor could be attributed to the high surface area and porosity of the sensing materials. The large surface area provides several active sites for oxygen adsorption and forms a high density of oxygen radicals on the surface of the sensing material [64]. Further, the NSC@ZNS sensor showed excellent sensitivity to $NO_2$ ~31 times higher than other gases such as $H_2S$, $NH_3$, $CH_4$, CO, and $H_2$. The electron-donating or reducing nature of as $H_2S$, $NH_3$, $CH_4$, CO, and $H_2$ cannot effectively adsorb on the nitrogen-sulfur doped carbon as compared to that of $NO_2$, thus showed weak sensing response. Nevertheless, the valid justification for selective $NO_2$ sensing continues to be uncertain and needs to be confirmed by further studies. The proposed NSC@ZNS sensor showed completely reversible sensing characteristics at 25 °C. The sensitivity of the NSC@ZNS sensor at 25 °C was found to be ~500 ppb with the LOD of ~21 ppb. Since the synergy between the $NO_2$ and the lone pair of electrons in NSC is weak, the $NO_2$ molecules can be desorbed from the NSC@ZNS nanocomposites by flowing dry air [64]. The proposed sensor showed excellent sensitivity, selectivity with appreciably fast response, and recovery time compared to the other reported $NO_2$ sensors (Table 1.).

## 5. Conclusions

In summary, we have developed a nitrogen-sulfur dual doped carbon-coated ZnO nanospheres by a facile hydrothermal and subsequent annealing process. The successful formation of the hybrid nanocomposite was confirmed by the various analytical techniques. The sensors were fabricated based on the as-synthesized materials and investigated in detail their $NO_2$ sensing at different temperatures and concentrations. The maximum sensitivity limit of the ZNS sensor was ~30 ppb at 225 °C. However, the ZNS sensor could not be able to detect $NO_2$ below 100 °C. Whereas, the NSC@ZNS and SC@ZNS, NC@ZNS hybrid sensors showed the excellent selectivity and sensitivity to $NO_2$ at ambient temperatures. Besides, all three sensors can naturally recover to their initial resistance value without any external source such as UV-light illumination or thermal assistance. The NSC@ZNS hybrid nanocomposite sensor showed ~1.5 and 1.15 times higher sensitivity compared to NC@ZNS, SC@ZNS sensors. The sensing characteristics of the sensors showed exceptional linear relationships in a wide range of $NO_2$ concentrations. The LOD of the NSC@ZNS, SC@ZNS and NC@ZNS sensors were found to be ~28 ppb, 25 ppb and 21 ppb, respectively. The NSC@ZNS sensor also showed ~31 times higher $NO_2$ sensing response compared to that of other gases. The facile fabrication, ultra-sensitive, and selective detection of $NO_2$ with appreciably fast response and recovery time at ambient temperatures make for intriguing the promising practical applications of our proposed NSC@ZNS sensor.

**Table 1**
$NO_2$ sensing characteristics of NSC@ZNS sensor and that of other reported $NO_2$ sensors.

| Sensing material | $T_S^a$ | $G_C^b$ | $S_R^c$ | $\Gamma_{RES}/\Gamma_{REC}^d$ | Ref. |
|---|---|---|---|---|---|
| S-Graphene | RT | 5 | 5 | 10/30 | Yuan *et al.* [65]. |
| $NbS_2$ | 27 | 5 | 1.5 | 3000/9000 | Kim *et al.* [66]. |
| $Cu_3Mo_2O_9$@CuO | RT | 5 | 1.6 | 49/241 | Adamu *et al.* [67]. |
| $WO_3$/S-RGO | RT | 20 | 1.5 | 6/56 | Wang *et al.* [68]. |
| Graphene/α-$Fe_2O_3$ | RT | 5 | 7.2 | 126/2400 | Zhang *et al.* [69]. |
| $SnO_{2-x}$ | RT | 5 | 16 | 331/1057 | Zhong *et al.* [70]. |
| AgNP-3D-AQRGO | RT | 20 | 10.3 | 300/600 | Li *et al.* [71] |
| NSC@ZNS | RT | 5 | 31.2 | 88/305 | This work |

[a]Sensing Temperature [a]Gas Concentration [c]Sensor Response (Rg/Ra or Ra/Rg) [d]Response and recovery time

## Declaration of Competing Interest

The authors declare that they have no known competing financial interests or personal relationships that could have appeared to influence the work reported in this paper.

## Acknowledgements

This work was financially supported by the National Research Foundation of Korea (NRF) grant funded by the Korean government (MSIT) (No. 2020R1A5A8018367) and Basic Science Research Pro-gram through the National Research Foundation of Korea (NRF) funded by the Ministry of Education (No. 2020R1I1A1A01073562).

## Appendix A. Supplementary data

Electronic supplementary information available

Preparation of sulfur doped carbon@ ZnO spheres (SC@ZNS). Preparation of nitrogen doped carbon@ ZnO spheres (NC@ZNS). Details of the experimental methods and characterization techniques. Gas sensors fabrication and measurement techniques. Fig. S1. Morphology of the as prepared SC@ZNS. Fig. S2. Elemental mapping of the as-prepared SC@ZNS hybrid nanocomposite. Fig. S3. Morphology of the as-prepared NC@ZNS hybrid nanocomposite. Fig. S4. Enlarged region of powder X-ray diffraction pattern of the as-prepared NC@ZS and NCS@ZS hybrid nanocomposites. Fig. S5. Thermal gravimetric profile of the as-prepared NC@ZNS, SC@ZNS and NSC@ZNS hybrid nanocomposite from room temperature to 900 °C at the heat rate of 10 °C/min. Fig. S6. $N_2$ adsorption–desorption Barrett–Joyner–Halenda (BJH) isotherms of the as-prepared ZNS, NC@ZNS, SC@ZNS and NSC@ZNS hybrid nanocomposites. Inset: the corresponding BJH pore size distributions from the adsorption branch. Fig. S7. Long-term stability of the fabricated sensor based on NSC@ZNS to 10 ppm of NO2 at 25 °C. Fig. S8. Response and recovery time of the fabricated sensor based on NC@ZNS and NSC@ZNS to 500 ppb of $NO_2$ at 25 °C. Fig. S9. Response and recovery time of the fabricated sensor based on SC@ZNS to 500 ppb of $NO_2$ at 25 °C. Fig. S10. The linear dependence of the logarithm of time constants versus the reverse of absolute temperature of the fabricated sensors

based on NC@ZNS, SC@ZNS and NSC@ZNS. Fig. S11. Sensor response of the NSC@ZNS to different relative humidity at 25 °C. Table S1. Atomic percentage (at. %) of carbon, oxygen, nitrogen, and zinc in the NC@ZNS, SC@ZNS and NSC@ZNS hybrid nanocomposites. Table S2. Comparison between surface and bulk elemental compositions of carbon, oxygen, nitrogen, and zinc in the NC@ZNS, SC@ZNS and NSC@ZNS hybrid nanocomposites.

Supplementary data to this article can be found online at https://doi.org/10.1016/j.cej.2020.127740.

## References


[1] J. Kong, N.R. Franklin, C. Zhou, M.G. Chapline, S. Peng, K. Cho, H. Dai, Nanotube molecular wires as chemical sensors, Science 287 (2000) 622–625.

[2] M. Ammann, M. Kalberer, D.T. Jost, L. Tobler, E. Rossler, D. Piguet, H.W. Gaggeler, U. Baltensperger, Heterogeneous production of nitrous acid on soot in polluted air masses, Nature 395 (1998) 157–160.

[3] J. Wu, Z. Wu, H. Ding, X. Yang, Y. Wei, M. Xiao, Z. Yang, B.-R. Yang, C. Liu, X. Lu, L. Qiu, X. Wang, Three-dimensional-structured boron- and nitrogen-doped graphene hydrogel enabling high-sensitivity $NO_2$ detection at room temperature, ACS Sens. 4 (2019) 1889–1898.

[4] J. Wu, Z. Li, X. Xie, K. Tao, C. Liu, K.A. Khor, J. Miao, L.K. Norford, 3D superhydrophobic reduced graphene oxide for activated $NO_2$ sensing with enhanced immunity to humidity, J. Mater. Chem. A. 6 (2018) 478–488.

[5] Z. Dai, C.S. Lee, Y. Tian, I.-D. Kim, J.-H. Lee, Highly reversible switching from P- to N-type $NO_2$ sensing in a monolayer $Fe_2O_3$ inverse opal film and the associated P-N transition phase diagram, J. Mater. Chem. A 3 (2015) 3372–3381.

[6] H. Fei, Enhanced $NO_2$ sensing at room temperature with graphene via monodisperse polystyrene bead decoration, ACS Omega. 4 (2019) 3812–3819.

[7] N.D. Hoa, S.A. El-Safty, Synthesis of mesoporous NiO nanosheets for the detection of toxic $NO_2$ Gas, Chem. Eur. J. 17 (2011) 12896–12901.

[8] M.M. Rana, D.S. Ibrahim, M.R. Mohd Asyraf, S. Jarin, A. Tomal, A review on recent advances of CNTs as gas sensors, Sens. Rev. 37 (2017) 127–136.

[9] F. Schedin, A.K. Geim, S.V. Morozov, E.W. Hill, P. Blake, M.I. Katsnelson, K. S. Novoselov, Detection of individual gas molecules adsorbed on graphene, Nat. Mater. 6 (2007) 652–655.

[10] N.A. Isaac, M. Valenti, A. Schmidt-Ott, G. Biskos, G. Characterization of tungsten oxide thin Films produced by spark ablation for $NO_2$ gas sensing, ACS Appl. Mater. Interfaces 8 (2016) 3933–3939.

[11] S. Roso, C. Bittencourt, P. Umek, O. Gonzalez, F. Guell, A. Urakawa, E. Llobet, Synthesis of single crystalline $In_2O_3$ octahedra for the selective detection of $NO_2$ and $H_2$ at trace levels, J. *Mater. Chem. C* 4 (2016) 9418–9427.

[12] G. Meng, F. Zhuge, K. Nagashima, A. Nakao, M. Kanai, Y. He, M. Boudot, T. Takahashi, K. Uchida, T. Yanagida, Nanoscale thermal management of single $SnO_2$ nanowire: pico-Joule energy consumed molecule sensor, ACS Sens. 1 (2016) 997–1002.

[13] S. Maeng, S.-W. Kim, D.-H. Lee, S.-E. Moon, K.-C. Kim, A. Maiti, $SnO_2$ nanoslab as $NO_2$ sensor: identification of the $NO_2$ sensing mechanism on a $SnO_2$ surface, ACS Appl. Mater. Interfaces 6 (2014) 357–363.

[14] H. Song, T. Chen, X. Zhang, X. Jia, One-step template-free synthesis of hollow core–shell α-$Fe_2O_3$ microspheres with improved lithium storage and gas-sensing properties, CrystEngComm 17 (2015) 1173–1181.

[15] M. Procek, A. Stolarczyk, T. Pustelny, Impact of temperature and UV irradiation on dynamics of $NO_2$ sensors based on ZnO nanostructures, Nanomaterials. 7 (2017) 312.

[16] W. Yang, P. Wan, X. Zhou, J. Hu, Y. Guan, L. Feng, Additive-free synthesis of $In_2O_3$ cubes embedded into graphene sheets and their enhanced $NO_2$ sensing performance at room temperature, ACS App. Mater. Interfaces 6 (2014) 21093–21100.

[17] X. Wang, S. Fazhe, D. Yongqing, Y. Zhouping, L. Wei, H. YongAn, C. Jiankui, Highly sensitive, temperature-dependent gas sensor based on hierarchical ZnO nanorod arrays, J. Mater. Chem. C 3 (2015) 11397–11405.

[18] T. Athanasios, K. Kiprono, T. Dimitrios, C. Davide, C. Giancarlo, P. Daniele, $NO_2$ Gas Sensing Mechanism of ZnO Thin-Film Transducers: Physical Experiment and Theoretical Correlation Study, ACS Sens. 1 (2016) 406–412.

[19] Xu, et al., New strategy towards the assembly of hierarchical heterostructures of $SnO_2$/ZnO for $NO_2$ detection at a ppb level, Inorg. Chem. Front. 6 (2019) 2801–2809.

[20] Z. Yong-Hui, L. Yu-Liang, G. Fei-Long, X. Ke-Fei, L. Min, Z. Hao-Li, F. Shao-Ming, Al doped narcissus-like ZnO for enhanced $NO_2$ sensing performance: An experimental and DFT investigation, Sens. Actuator B-Chem. 305 (2020), 127489.

[21] A. Shanmugasundaram, N.D. Chinh, Y.-J. Jeong, T.F. Hou, D.-S. Kim, D. Kim, Y.-B. Kim, D.-W. Lee, Hierarchical nanohybrids of B- and N-codoped graphene/mesoporous NiO nanodisks: an exciting new material for selective sensing of H2S at near ambient temperature, J. Mater. Chem. A 7 (2019) 9263–9278.

[22] E. Pargoletti, U.H. Hossain, I.D. Bernardo, H. Chen, T. Tran-Phu, J. Lipton-Duffin, G. Cappelletti, A. Tricoli, Room-temperature photodetectors and VOC sensors based on graphene oxide–ZnO nanoheterojunctions, Nanoscale 11 (2019) 22932–22945.

[23] J. Wang, Y. Shena, X. Li, Y. Xia, C. Yang, Synergistic effects of UV activation and surface oxygen vacancies on the room-temperature $NO_2$ gas sensing performance of ZnO nanowires, Sens. Actuators B Chem. 298 (2019), 126858.

[24] E. Espid, F. Taghipour, UV-LED photo-activated chemical gas sensors: a review. critical reviews in solid-state and materials sciences. 42 (2017) 416–432.

[25] S. Zhao, Y. Shen, P. Zhou, X. Zhong, C. Han, Q. Zhao, D. Wei, Design of Au@$WO_3$ core−shell structured nanospheres for ppb-level $NO_2$ sensing, Sens. Actuator B Chem. 282 (2019) 917–926.

[26] Y. Liu, X. Gao, F. Li, G. Lu, T. Zhang, N. Barsan, N. Pt-$In_2O_3$ mesoporous nanofibers with enhanced gas sensing performance towards ppb-level $NO_2$ at room temperature, Sens. Actuator B Chem. 260 (2018) 927–936.

[27] Z. Wang, G. Men, R. Zhang, F. Gu, D. Han, Pd loading induced excellent $NO_2$ gas sensing of 3DOM $In_2O_3$ at room temperature, Sens. Actuator B Chem. 263 (2018) 218–228.

[28] Q. Zhang, G. Xie, M. Xu, Y. Su, H. Tai, H. Du, Y. Jiang, Visible light-assisted room temperature gas sensing with ZnO-Ag heterostructure nanoparticles, Sens. Actuator B Chem. 259 (2018) 269–281.

[29] A. Shanmugasundaram, V. Gundimeda, T.F. Hou, D.-W. Lee, Realizing synergy between $In_2O_3$ nanocubes and nitrogen-doped reduced graphene Oxide: An excellent nanocomposite for the selective and sensitive detection of CO at ambient temperatures, ACS Appl. Mater. Interfaces 9 (2017) 31728–31740.

[30] L. Huang, Z. Wang, J. Zhang, J. Pu, Y. Lin, S. Xu, L. Shen, Q. Chen, W. Shi, Fully Printed, Rapid-Response Sensors Based on Chemically Modified Graphene for Detecting $NO_2$ at Room Temperature, ACS App. Mater. Interfaces 6 (2014) 7426–7433.

[31] R. Lv, et al., Ultrasensitive gas detection of large-area boron-doped graphene, Proc. Natl. Acad. Sci. 112 (2015) 14527–14532.

[32] J. Wu, K. Tao, Y. Guo, Z. Li, X. Wang, Z. Luo, S. Feng, C. Du, D. Chen, J. Miao, L. K. Norford, A 3D chemically modified graphene hydrogel for fast, highly sensitive, and selective gas sensor, Adv. Sci. 4 (2017) 1600319.

[33] J. Li, H. Zhao, M. Wang, Y. Zhu, B. Li, X. Yu, J. Xu, Y. Cheng, L. Ouyang, H. Shao, Rational design of 3D N-doped carbon nanosheet framework encapsulated ultrafine ZnO nanocrystals as superior performance anode materials in lithium ion batteries, J. Mater. Chem. A 7 (2019) 25155–25164.

[34] S. Arunkumar, T.F. Hou, Y.-B. Kim, B. Choi, S.H. Park, S. Jung, D.-W. Lee, Au Decorated ZnO hierarchical architectures: Facile synthesis, tunable morphology and enhanced CO detection at room temperature, Sens. Actuators B Chem. 243 (2017) 990–1001.

[35] H.-Y. Kim, N. Saito, D. Kim, Enhancing Bifunctional Catalytic Activity of Oxygen Reduction and Evolution Reaction via One-Pot Formation of $MnO_2$-Carbon Hybrid Nanocomposite, ChemistrySelect 3 (2018) 6302–6308.

[36] S. Li, C. Zhao, S. Zhou, Y. Zhang, P. Zhu, J. Yu, Non-covalent interaction-driven self-assembly of perylene diimide on rGO for room-temperature sensing of triethylamine with enhanced immunity to humidity, Chem. Eng. J. 385 (2020), 123397.

[37] Y. Guo, S. Yao, L. Gao, A. Chen, M. Jiao, H. Cui, Z. Zhou, Boosting bifunctional electrocatalytic activity in S and N co-doped carbon nanosheets for high-efficiency Zn-air batteries, J. Mater. Chem. A (2020).

[38] F. Wu, J. Li, Y. Tian, Y. Su, J. Wang, W. Yang, N. Li, S. Chen, L. Bao, 3D coral-like nitrogen-sulfur codoped carbon-sulfur composite for high performance lithium-sulfur batteries, Scientific Reports 5 (2015) 13340.

[39] V.K. Abdelkader-Fernández, D.M. Fernandes, S.S. Balula, L. Cunha-Silva, M. J. Pérez-Mendoza, F.J. López-Garzón, M.F. Pereira, C. Freire, Noble-Metal-Free MOF-74-Derived nanocarbons: insights on metal composition and doping effects on the electrocatalytic activity toward oxygen reactions, ACS Appl. Energy Mater. 2 (2019) 1854–1867.

[40] A. Shanmugasundaram, R. Boppella, Y.-J. Jeong, J. Park, Y.-B. Kim, B. Choi, S. H. Park, S. Jung, D.-W. Lee, Facile in-situ formation of rGO/ZnO nanocomposite: Photocatalytic remediation of organic pollutants under solar illumination, Mater. Chem. Phy. 218 (2018) 218–228.

[41] S. Chen, X. Zhou, J. Liao, S. Yang, X. Zhou, Q. Gao, S. Zhang, Y. Fang, X. Zhong, S. Zhang, FeNi Intermetallic Compound Nanoparticles Wrapped by N-doped Graphitized Carbon: A novel Cocatalyst for Boosting Photocatalytic Hydrogen Evolution, J. Mater. Chem. A 8 (2020) 3481–3490.

[42] W. Li, M. Zhou, H. Li, K. Wang, S. Cheng, K. Jiang, High Performance Sulfur-doped Disordered Carbon Anode for Sodium Ion Batteries, Energy Environ. Sci. 8 (2015) 2916–2921.

[43] J. Yan, W. Li, P. Feng, R. Wang, M. Jiang, J. Han, S. Cao, K. Wang, K. Jiang, Enhanced $Na^+$ pseudocapacitance in a P, S codoped carbon anode arising from the surface modification by sulfur and phosphorus with C-S–P coupling, J. Mater. Chem. A 8 (2020) 422–432.

[44] Z. Dai, K. Liu, Y. Tang, X. Yang, J. Bao, J. Shen, A novel tetragonal pyramid-shaped porous ZnO nanostructure and its application in the biosensing of horseradish peroxidise, J. Mater. Chem. 18 (2008) 1919–1926.

[45] P. Cao, Y. Cai, D. Pawar, S.T. Navale, C.N. Rao, S. Han, W.Y. Xu, M. Fang, X. Liu, Y. X. Zeng, W.J. Liu, D.L. Zhu, Down to ppb level $NO_2$ detection by ZnO/rGO heterojunction based chemiresistive sensors, Chem. Eng. J. 401 (2020), 125491.

[46] H. Song, S. Yan, Y. Yao, L. Xia, X. Jia, J. Xu, 3Dα-Fe2$O_3$ nanorods arrays@graphene oxide nanosheets as sensing materials for improved gas sensitivity, Chem. Eng. J. 319 (2019) 1331–1340.

[47] H. Ding, J.-S. Wei, H.-M. Xiong, Nitrogen and sulfur co-doped carbon dots with strong blue luminescence, Nanoscale. 6 (2014) 13817–13823.

[48] W. Li, Z. Zhang, B. Kong, S. Feng, J. Wang, L. Wang, J. Yang, F. Zhang, P. Wu, D. Zhao, Angew. Chem., Int. Ed. 52 (2013) 8151.

[49] A. Shanmugasundaram, B. Ramireddy, P. Basak, S.V. Manorama, S. Srinath, Hierarchical In (OH) 3 as a precursor to mesoporous $In_2O_3$ nanocubes: a facile synthesis route, mechanism of self-assembly, and enhanced sensing response toward hydrogen, J. Phys. Chem. 118 (2014) 6909–6921.

[50] A. Shanmugasundaram, P. Basak, S.V. Manorama, B. Krishna, S. Sanyadanam, Hierarchical mesoporous $In_2O_3$ with enhanced CO sensing and photocatalytic performance: distinct morphologies of $In(OH)_3$ via self assembly coupled in situ solid–solid transformation, ACS Appl. Mater. Interfaces 7 (2015) 7679–7689.
[51] A. Shanmugasundaram, P. Basak, L. Satyanarayana, S.V. Manorama, Hierarchical SnO/$SnO_2$ nanocomposites: Formation of in situ p–n junctions and enhanced $H_2$ sensing, Sens. Actuators B-Chem. 185 (2013) 265–273.
[52] J. Wu, K. Tao, J. Miao, L.K. Norford, Improved Selectivity and Sensitivity of Gas Sensing Using a 3D Reduced Graphene Oxide Hydrogel with an Integrated Microheater, ACS Appl. Mater. Interfaces 7 (2015) 27502–27510.
[53] V. Dua, S.P. Surwade, S. Ammu, S.R. Agnihotra, S. Jain, K.E. Roberts, S. Park, R. S. Ruoff, S.K. Manohar, All-Organic Vapor Sensor Using Inkjet-Printed Reduced Graphene Oxide, Angew. Chem., Int. Ed. 49 (2010) 2154–2157.
[54] L. Xu, B. Dong, Y. Wang, X. Bai, Q. Liu, H.W. Song, Electrospinning preparation and room temperature gas sensing properties of porous $In_2O_3$ nanotubes and nanowires, Sens. Actuat. B-Chem. 147 (2010) 531–538.
[55] L. Xu, R. Zheng, S. Liu, J. Song, J. Chen, B. Dong, H. Song, NiO@ZnO Heterostructured Nanotubes: Coelectrospinning Fabrication, Characterization, and Highly Enhanced Gas Sensing Properties, Inorg. Chem. 51 (2012) 7733–7740.
[56] C.T. Quy, N.X. Thai, N.D. Hoa, D.T.T. Le, C.M. Hung, N.V. Duy, N.V. Hieu, $C_2H_5OH$ and $NO_2$ sensing properties of ZnO nanostructures: correlation between crystal size, defect level and sensing performance, RSC Adv. 8 (2018) 5629–5639.
[57] H. Wang, W. Fu, X. Yang, Z. Huang, J. Li, H. Zhang, Y. Wang, Recent advancements in heterostructured interface engineering for hydrogen evolution reaction electrocatalysis, J. Mater. Chem. A (2020), https://doi.org/10.1039/C9TA11646J.
[58] X. Wang, et al., One-pot synthesis of nitrogen and sulfur co-doped graphene as efficient metal-free electrocatalysts for the oxygen reduction reaction, Chem. Commun. 50 (2014) 4839–4842.
[59] Y. She, Z. Lu, M. Ni, L. Li, N.K.H. Leung, Facile Synthesis of nitrogen and sulfur codoped carbon from ionic liquid as metal-free catalyst for oxygen reduction reaction, ACS Appl. Mater. Interfaces 7 (2015) 7214–7221.
[60] R. Ma, G. Lin, Y. Zhou, Q. Liu, T. Zhang, G. Shan, M. Yang, J. Wang, A review of oxygen reduction mechanisms for metal-free carbon-based electrocatalysts, Npj Comput. Mater. 5 (2019) 78.
[61] R. Bo, One-Step Synthesis of Porous Transparent Conductive Oxides by Hierarchical Self-Assembly of Aluminium-Doped ZnO Nanoparticles, ACS Appl. Mater. Interfaces (2020), https://doi.org/10.1021/acsami.9b19423.
[62] Y. Wang, R. Xu, L. Chen, C. Wu, L. Qiu, C.D. Windle, Q. Han, L. Qu, Hierarchical ZnO@Hybrid Carbon Core−Shell Nanowire Array on a Graphene Fiber Microelectrode for Ultrasensitive Detection of 2,4,6- Trinitrotoluene, ACS Appl. Mater. Interfaces (2020), https://doi.org/10.1021/acsami.9b20296.
[63] J. Dai, J. Yuan, P. Giannozz, Gas adsorption on graphene doped with B, N, Al, and S: A theoretical study, Appl. Phys. Lett. 95 (2009), 232105.
[64] K. Watanabe, K. Matsumoto, T. Ohgaki, I. Sakaguchi, N. Ohashi, S. Hishita, H. Haneda, Development of ZnO-based surface plasmon resonance gas sensor and analysis of UV irradiation effect on $NO_2$ desorption from ZnO thin films, J. Ceram. Soc. Jpn. 118 (2010) 193–196.
[65] C. Li, X. Qiao, J. Jiam, F. Feng, H. Wang, L. Jia, Ordered porous $BiVO_4$ based gas sensors with high selectivity and fast-response towards $H_2S$, Chem. Eng. J. 375 (2019), 121924.
[66] W. Yuan, A. Liu, L. Huang, C. Li, G. Shi, High-Performance $NO_2$ Sensors Based on Chemically Modified Graphene, Adv. Mater. 25 (2013) 766–771.
[67] Y. Kim, et al., Two-Dimensional $NbS_2$ Gas Sensors for Selective and Reversible $NO_2$ Detection at Room Temperature, ACS Sens. 4 (2019) 2395–2402.
[68] B.S. Adamu, A. Falak, Y. Tian, X. Tan, X. Meng, P. Chen, H. Wang, W. Chu, p–p Heterojunction Sensors of *p*-$Cu_3Mo_2O_9$ Micro/Nanorods Vertically Grown on *p*-CuO Layers for Room-Temperature Ultrasensitive and Fast Recoverable Detection of $NO_2$, ACS Appl. Mater. Interfaces (2020), https://doi.org/10.1021/acsami.9b19971.
[69] T. Wang, J. Hao, S. Zheng, Q. Sun, D. Zhang, Y. Wang, Highly Sensitive and Rapidly Responding Room-Temperature $NO_2$ Gas Sensors Based on $WO_3$ Nanorods /Sulfonated Graphene Nanocomposites, Nano Res. 11 (2018) 791–803.
[70] B. Zhang, G. Liu, M. Cheng, Y. Gao, L. Zhao, S. Li, F. Liu, X. Yan, T. Zhang, P. Sun, G.Y. Lu, The Preparation of Reduced Graphene Oxide-Encapsulated a-$Fe_2O_3$ Hybrid and Its Outstanding $NO_2$ Gas Sensing Properties at Room Temperature, Sens. Actuators. B 261 (2018) 252–263.
[71] Y. Zhong, W.W. Li, X. Zhao, X. Jiang, S. Lin, Z. Zhen, W. Chen, D. Xie, H. Zhu, High-Response Room-Temperature $NO_2$ Sensor and Ultrafast Humidity Sensor Based on $SnO_2$ with Rich Oxygen Vacancy, ACS Appl. Mater. Interfaces 11 (2019) 13441–13449.